

1 High-level cognition during story listening is reflected in
2 high-order dynamic correlations in neural activity patterns

3 Lucy L. W. Owen¹, Thomas H. Chang^{1,2}, and Jeremy R. Manning^{1,†}

¹Department of Psychological and Brain Sciences,
Dartmouth College, Hanover, NH

²Amazon.com, Seattle, WA

†Address correspondence to jeremy.r.manning@dartmouth.edu

4 November 13, 2020

5 **Abstract**

6 Our thoughts arise from coordinated patterns of interactions between brain structures that change with
7 our ongoing experiences. High-order dynamic correlations in neural activity patterns reflect different sub-
8 graphs of the brain's functional connectome that display homologous lower-level dynamic correlations. We
9 tested the hypothesis that high-level cognition is supported by reflected in high-order dynamic correlations
10 in brain activity patterns. We developed an approach to estimating high-order dynamic correlations in
11 timeseries data, and we applied the approach to neuroimaging data collected as human participants either
12 listened to a ten-minute story or listened to a temporally scrambled version of the story, or underwent
13 a resting-state scan. We trained across-participant pattern classifiers to decode (in held-out data) when in
14 the session each neural activity snapshot was collected. We found that classifiers trained to decode from
15 high-order dynamic correlations yielded the best performance on data collected as participants listened
16 to the (unscrambled) story. By contrast, classifiers trained to decode data from scrambled versions of the
17 story or during the resting state scan yielded the best performance when they were trained using first-
18 order dynamic correlations or non-correlational activity patterns. We suggest that as our thoughts become
19 more complex, they are supported by reflected in higher-order patterns of dynamic network interactions
20 throughout the brain.

21 **Introduction**

22 A central goal in cognitive neuroscience is to elucidate the *neural code*: the mapping between (a) mental
23 states or cognitive representations and (b) neural activity patterns. One means of testing models of the
24 neural code is to ask how accurately that model is able to "translate" neural activity patterns into known
25 (or hypothesized) mental states or cognitive representations (e.g., Haxby et al., 2001; Huth et al., 2016, 2012;
26 Kamitani & Tong, 2005; Mitchell et al., 2008; Nishimoto et al., 2011; Norman et al., 2006; Pereira et al.,
27 2018; Tong & Pratte, 2012). Training decoding models on different types of neural features (Fig. 1a) can
28 also help to elucidate which specific aspects of neural activity patterns are informative about cognition—
29 and, by extension, which types of neural activity patterns might comprise compose the neural code. For
30 example, prior work has used region of interest analyses to estimate the anatomical locations of specific

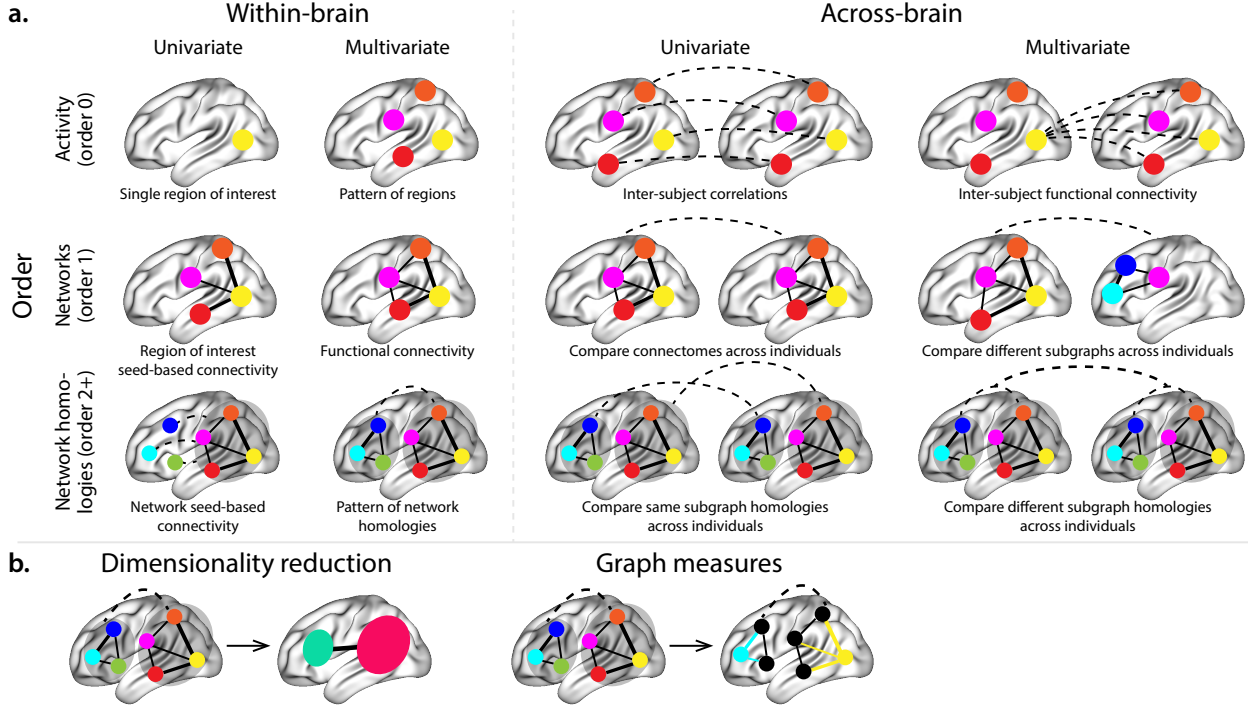


Figure 1: Neural patterns. a. A space of neural features. Within-brain analyses are carried out within a single brain, whereas across-brain analyses compare neural patterns across two or more individuals' brains. Univariate analyses characterize the activities of individual units (e.g., nodes, small networks, hierarchies of networks, etc.), whereas multivariate analyses characterize the patterns of activities across units. Order 0 patterns involve individual nodes; order 1 patterns involve node-node interactions; order 2 (and higher) patterns relate to interactions between homologous networks. Each of these patterns may be static (e.g., averaging over time) or dynamic. **b. Summarizing neural patterns.** To efficiently compute with complex neural patterns, it can be useful to characterize the patterns using summary measures. Dimensionality reduction algorithms project the patterns onto lower-dimensional spaces whose dimensions reflect weighted combinations or non-linear transformations of the dimensions in the original space. Graph measures characterize each unit's participation in its associated network.

31 neural representations (e.g., Etzel et al., 2009), or to compare the relative contributions to the neural code of
 32 multivariate activity patterns versus dynamic correlations between neural activity patterns (e.g., Fong et al.,
 33 2019; Manning et al., 2018). An emerging theme in this literature is that cognition is mediated by dynamic
 34 interactions between brain structures (Bassett et al., 2006; Demertzi et al., 2019; Friston, 2000; Grossberg,
 35 1988; Lurie et al., 2018; Mack et al., 2017; Preti et al., 2017; Solomon et al., 2019; Sporns & Honey, 2006;
 36 Turk-Browne, 2013; Zou et al., 2019).

37 Studies of the neural code to date have primarily focused on univariate or multivariate neural pat-
 38 terns (for review see Norman et al., 2006), or (more recently) on patterns of dynamic first-order corre-
 39 lations (i.e., interactions between pairs of brain structures; Demertzi et al., 2019; Fong et al., 2019; Lurie et al.,
 40 2018; Manning et al., 2018; Preti et al., 2017; Zou et al., 2019). **We wondered what What might** the future

41 of this line of work ~~might hold~~. hold? For example, is the neural code ~~mediated by~~ implemented through
42 higher-order interactions between brain structures (e.g., see Reimann et al., 2017)? Second-order correlations
43 reflect *homologous* patterns of correlation. In other words, if the dynamic patterns of correlations between
44 two regions, *A* and *B*, are similar to those between two other regions, *C* and *D*, this would be reflected
45 in the second-order correlations between (*A*-*B*) and (*C*-*D*). In this way, second-order correlations identify
46 similarities and differences between subgraphs of the brain’s connectome. Analogously, third-order cor-
47 relations reflect homologies between second-order correlations—i.e., homologous patterns of homologous
48 interactions between brain regions. More generally, higher-order correlations reflect homologies between
49 patterns of lower-order correlations. We can then ask: which “orders” of interaction are most reflective of
50 high-level cognitive processes?

51 One reason one might expect to see homologous networks in a dataset is related to the notion that
52 network dynamics reflect ongoing neural computations or cognitive processing (e.g., Beatty et al., 2016). If
53 the nodes in two brain networks are interacting (within each network) in similar ways then, according to
54 our characterization of network dynamics, we refer to the similarities between those patterns of interaction
55 as higher-order correlations. When higher-order correlations are themselves changing over time, we can
56 also attempt to capture and characterize those high-order dynamics.

57 Another central question pertains to the extent to which the neural code is carried by activity patterns
58 that directly reflect ongoing cognition (e.g., following Haxby et al., 2001; Norman et al., 2006), versus the
59 dynamic properties of the network structure itself, independent of specific activity patterns in any given
60 set of regions (e.g., following Bassett et al., 2006). For example, graph measures such as centrality and
61 degree (Bullmore & Sporns, 2009) may be used to estimate how a given brain structure is “communicating”
62 with other structures, independently of the specific neural representations carried by those structures.
63 If one considers a brain region’s position in the network (e.g., its eigenvector centrality) as a dynamic
64 property, one can compare how the positions of different regions are correlated, and/or how those patterns
65 of correlations change over time. We can also compute higher-order patterns in these correlations to
66 characterize homologous subgraphs in the connectome that display similar changes in their constituent
67 brain structures’ interactions with the rest of the brain.

68 To gain insights into the above aspects of the neural code, we developed a computational framework
69 for estimating dynamic high-order correlations in timeseries data. This framework provides an important
70 advance, in that it enables us to examine patterns of higher-order correlations that are computationally
71 intractable to estimate via conventional methods. Given a multivariate timeseries, our framework provides
72 timepoint-by-timepoint estimates of the first-order correlations, second-order correlations, and so on. Our
73 approach combines a kernel-based method for computing dynamic correlations in timeseries data with a di-

74 dimensionality reduction step (Fig. 1b) that projects the resulting dynamic correlations into a low-dimensional
75 space. We explored two dimensionality reduction approaches: principle components analysis (PCA; Pearson,
76 1901), which preserves an approximately invertible transformation back to the original data (e.g., this
77 follows related approaches taken by Gonzalez-Castillo et al., 2019; McIntosh & Jirsa, 2019; Toker & Som-
78 mer, 2019); and a second non-invertible algorithm that explored patterns in eigenvector centrality (Landau,
79 1895). This latter approach characterizes correlations between each feature dimension's relative *position* in
80 the network in favor of the specific activity histories of different features (also see Betzel et al., 2019; Reimann
81 et al., 2017; Sizemore et al., 2018).

82 We validated our approach using synthetic data where the underlying correlations were known. We then
83 applied our framework to a neuroimaging dataset collected as participants listened to either an audio record-
84 ing of a ten-minute story, listened to a temporally scrambled version of the story, or underwent a resting state
85 scan (Simony et al., 2016). Temporal scrambling has been used in a growing number of studies, largely by Uri
86 Hasson's group, to identify brain regions that are sensitive to higher-order and longer-timescale information
87 (e.g., cross-sensory integration, rich narrative meaning, complex situations, etc.) versus regions that are
88 primarily sensitive to low-order (e.g., sensory) information. For example, Hasson et al. (2008) argues that
89 when brain areas are sensitive to fine versus coarse temporal scrambling, this indicates that they are "higher
90 order" in the sense that they process contextual information pertaining to further-away timescales. By
91 contrast, low-level regions, such as primary sensory cortices, do not meaningfully change their responses
92 (after correcting for presentation order) even when the stimulus is scrambled at fine timescales.

93 We used a subset of the story listening and rest data to train across-participant classifiers to decode
94 listening times (of groups of participants) using a blend of neural features (comprising neural activity
95 patterns, as well as different orders of dynamic correlations between those patterns that were inferred
96 using our computational framework). We found that both the PCA-based and eigenvector centrality-based
97 approaches yielded neural patterns that could be used to decode accurately (i.e., well above chance). Both
98 approaches also yielded the best decoding accuracy for data collected during (intact) story listening when
99 high-order (PCA: second-order; eigenvector centrality: fourth-order) dynamic correlation patterns were
100 included as features. When we trained classifiers on the scrambled stories or resting state data, only
101 (relatively) lower-order dynamic patterns were informative to the decoders. Taken together, our results
102 indicate that high-level cognition is supported by high-order dynamic patterns of communication between
103 brain structures.

104 **Results**

105 We sought to understand whether high-level cognition is reflected in dynamic patterns of high-order
106 correlations. To that end, we developed a computational framework for estimating the dynamics of
107 stimulus-driven high-order correlations in multivariate timeseries data (see *Dynamic inter-subject functional*
108 *connectivity (DISFC)* and *Dynamic higher-order correlations*). We evaluated the efficacy of this framework at
109 recovering known patterns in several synthetic datasets (see *Synthetic data: simulating dynamic first-order*
110 *correlations* and *Synthetic data: simulating dynamic higher-order correlations*). We then applied the framework
111 to a public fMRI dataset collected as participants listened to an auditorily presented story, listened to a
112 temporally scrambled version of the story, or underwent a resting state scan (see *Functional neuroimaging*
113 *data collected during story listening*). We used the relative decoding accuracies of classifiers trained on different
114 sets of neural features to estimate which types of features reflected ongoing cognitive processing.

115 Recovering known dynamic correlations from synthetic data

116 Recovering dynamic first-order correlations

117 We generated synthetic datasets that differed in how the underlying first-order correlations changed over
118 time. For each dataset, we applied Equation 4 with a variety of kernel shapes and widths. We assessed how
119 well the true underlying correlations at each timepoint matched the recovered correlations (Fig. 2). For every
120 kernel and dataset we tested, our approach recovered the correlation dynamics we embedded into the data.
121 However, the quality of these recoveries varied across different synthetic datasets in a kernel-dependent
122 way.

123 In general, wide monotonic kernel shapes (Laplace, Gaussian), and wider kernels (within a shape),
124 performed best when the correlations varied gradually from moment-to-moment (Figs. 2a, c, and d). In the
125 extreme, as the rate of change in correlations approaches 0 (Fig. 2a), an infinitely wide kernel would exactly
126 recover the Pearson's correlation (e.g., compare Eqns. 1 and 4).

127 When the correlation dynamics were unstructured in time (Fig. 2b), a Dirac δ kernel (infinitely narrow)
128 performed best. This is because, when every timepoint's correlations are independent of the correlations at
129 every other timepoint, averaging data over time dilutes the available signal. Following a similar pattern,
130 holding kernel shape fixed, narrower kernel parameters better recovered randomly varying correlations.

131 Recovering dynamic higher-order correlations

132 Following our approach to evaluating our ability to recover known dynamic first-order correlations from
133 synthetic data, we generated an analogous second set of synthetic datasets that we designed to exhibit
134 known dynamic first-order *and* second-order correlations (see *Synthetic data: simulating dynamic higher-order*

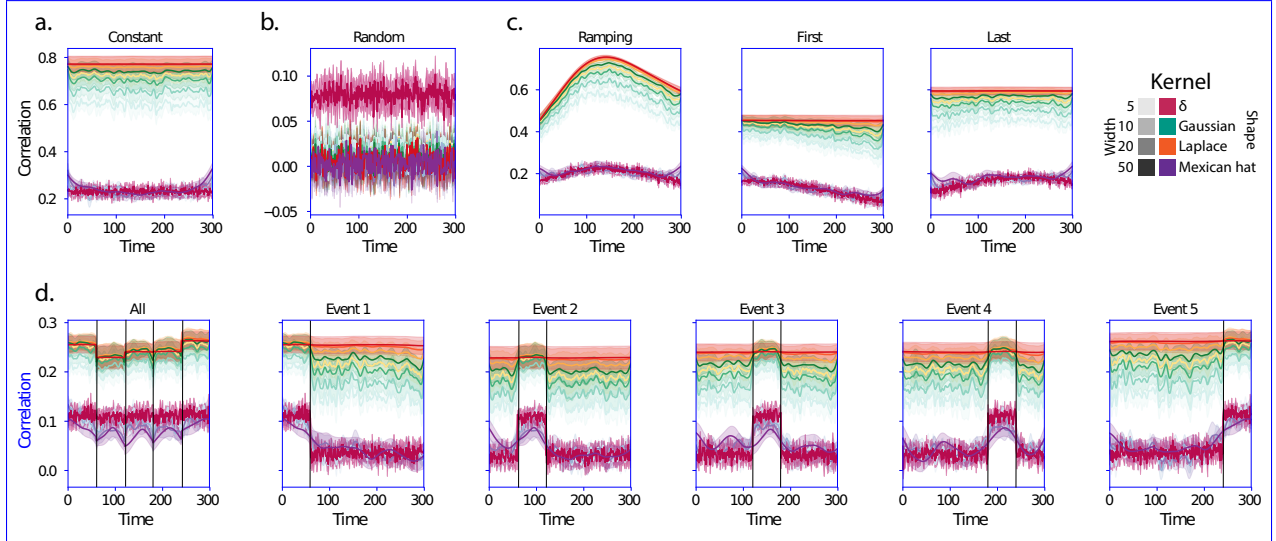


Figure 2: **Recovering known dynamic first-order correlations from synthetic data.** Each panel displays the average correlations between the vectorized upper triangles of the recovered correlation matrix at each timepoint and either the true underlying correlation at each timepoint or a reference correlation matrix. (The averages are taken across 10 different randomly generated synthetic datasets of the given category.) Error ribbons denote 95% confidence intervals (taken across datasets). Different colors denote different kernel shapes, and the shading within each color family denotes the kernel width parameter. For a complete description of each synthetic dataset, see *Synthetic data: simulating dynamic first-order correlations*.
a. Constant correlations. These datasets have a stable (unchanging) underlying correlation matrix.
b. Random correlations. These datasets are generated using a new independently drawn correlation matrix at each new timepoint.
c. Ramping correlations. These datasets are generated by smoothly varying the underlying correlations between the randomly drawn correlation matrices at the first and last timepoints. The left panel displays the correlations between the recovered dynamic correlations and the underlying ground truth correlations. The middle panel compares the recovered correlations with the *first* timepoint's correlation matrix. The right panel compares the recovered correlations with the *last* timepoint's correlation matrix.
d. Event-based correlations. These datasets are each generated using five randomly drawn correlation matrices that each remain stable for a fifth of the total timecourse. The left panel displays the correlations between the recovered dynamic correlations and the underlying ground truth correlations. The right panels compare the recovered correlations with the correlation matrices unique to each event. The vertical lines denote event boundaries.

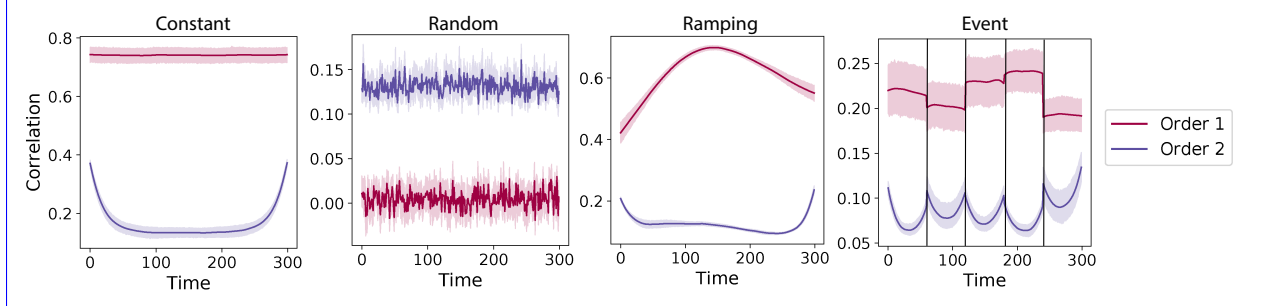


Figure 3: **Recovery of simulated first-order and second-order dynamic correlations.** Each panel displays the average correlations between the vectorized upper triangles of the recovered correlation matrix and the simulated correlation matrix at each timepoint and for each synthetic dataset. (The averages are taken across 10 different randomly generated synthetic datasets of the given category.) Error ribbons denote 95% confidence intervals (taken across datasets). For a complete description of each synthetic dataset, see *Synthetic data: simulating dynamic higher-order correlations*. All results in this figure used a Laplace kernel (width = 20). **a. Constant correlations.** These first and second order dynamic correlation were simulated from datasets have a stable (unchanging) underlying correlation matrix. **b. Random correlations.** These first and second order dynamic correlation were simulated from datasets are generated using a new independently drawn correlation matrix at each new timepoint. **c. Ramping correlations.** These first and second order dynamic correlation were simulated from datasets are generated by smoothly varying the underlying correlations between the randomly drawn correlation matrices at the first and last timepoints and displays the correlations between the recovered dynamic correlations and the simulated correlation first and second order correlation matrices. **d. Event-based correlations.** These first and second order dynamic correlation were simulated from datasets are each generated using five randomly drawn correlation matrices that each remain stable for a fifth of the total timecourse. The vertical lines denote event boundaries.

correlations). We generated a total of 40 datasets that varied in how the first-order and second-order correlations changed over time. We then repeatedly applied Equation 4 using the overall best-performing kernel from our first-order tests (a Laplace kernel with a width of 20; Fig. 2) to assess how closely the recovered dynamic correlations matched the dynamic correlations we had embedded into the datasets.

Overall, we found that we could reliably recover both first-order and second-order correlations from the synthetic data (Fig. 3). When the correlations were stable for longer intervals, or changed gradually (constant, ramping, and event datasets), recovery performance was relatively high, and we were better able to recover dynamic first-order correlations than second-order correlations. We expected that this would happen, given that errors in our estimation procedure at lower orders necessarily propagate to higher orders (since lower-order correlations are used to estimate higher-order correlations). Interestingly, we also found that when the correlations were particularly *unstable* (random datasets), we better recovered second-order correlations.

Taken together, our explorations using synthetic data indicated that we are able to partially, but not perfectly, recover ground truth dynamic first-order and second-order correlations. This suggests that our modeling approach provides a meaningful (if noisy) estimate of high-order correlations. We next turned to analyses of human fMRI data to examine whether the recovered dynamics might reflect the dynamics of

151 human cognition during a naturalistic story-listening task.

152 Cognitively relevant dynamic high-order correlations in fMRI data

153 We used across-participant temporal decoders to identify cognitively relevant neural patterns in fMRI data
154 (see *Forward inference and decoding accuracy*). The dataset we examined (collected by Simony et al., 2016)
155 comprised four experimental conditions that exposed participants to stimuli that varied systematically in
156 how cognitively engaging they were. The *intact* experimental condition had participants listen to an audio
157 recording of a 10-minute story. The *paragraph*-scrambled experimental condition had participants listen to a
158 temporally scrambled version of the story, where the paragraphs occurred out of order (but where the same
159 total set of paragraphs were presented over the full listening interval). All participants in this condition
160 experienced the scrambled paragraphs in the same order. The *word*-scrambled experimental condition had
161 participants listen to a temporally scrambled version of the story where the words in the story occurred in a
162 random order. All participants in the word condition experienced the scrambled words in the same order.
163 Finally, in a *rest* experimental condition, participants lay in the scanner with no overt stimulus, with their
164 eyes open (blinking as needed). This dataset provided a convenient means of testing our hypothesis that
165 different levels of cognitive processing and engagement are reflected in different orders of brain activity
166 dynamics.

167 In brief, we computed timeseries of dynamic high-order correlations that were similar across participants
168 in each of two randomly assigned groups: a training group and a test group. We then trained classifiers
169 on the training group's data to match each sample from the test group with a stimulus timepoint. Each
170 classifier comprised a weighted blend of neural patterns that reflected up to n^{th} -order dynamic correlations
171 (see *Feature weighting and testing*, Fig. 10). We repeated this process for $n \in \{0, 1, 2, \dots, 10\}$. Our examinations
172 of synthetic data suggested that none of the kernels we examined were “universal” in the sense of optimally
173 recovering underlying correlations regardless of the temporal structure of those correlations. We found a
174 similar pattern in the (real) fMRI data, whereby different kernels yielded different decoding accuracies, but
175 no single kernel emerged as the clear “best.” In our analyses of neural data, we therefore averaged our
176 decoding results over a variety of kernel shapes and widths in order to identify results that were robust to
177 specific kernel parameters (see *Identifying robust decoding results*).

178 Our approach to estimating dynamic high-order correlations entails mapping the high-dimensional
179 feature space of correlations (represented by a T by $O(K^2)$ matrix) onto a lower-dimensional feature space
180 (represented by a T by K matrix). We carried out two sets of analyses that differed in how this mapping was
181 computed. The first set of analyses used PCA to find a low-dimensional embedding of the original dynamic

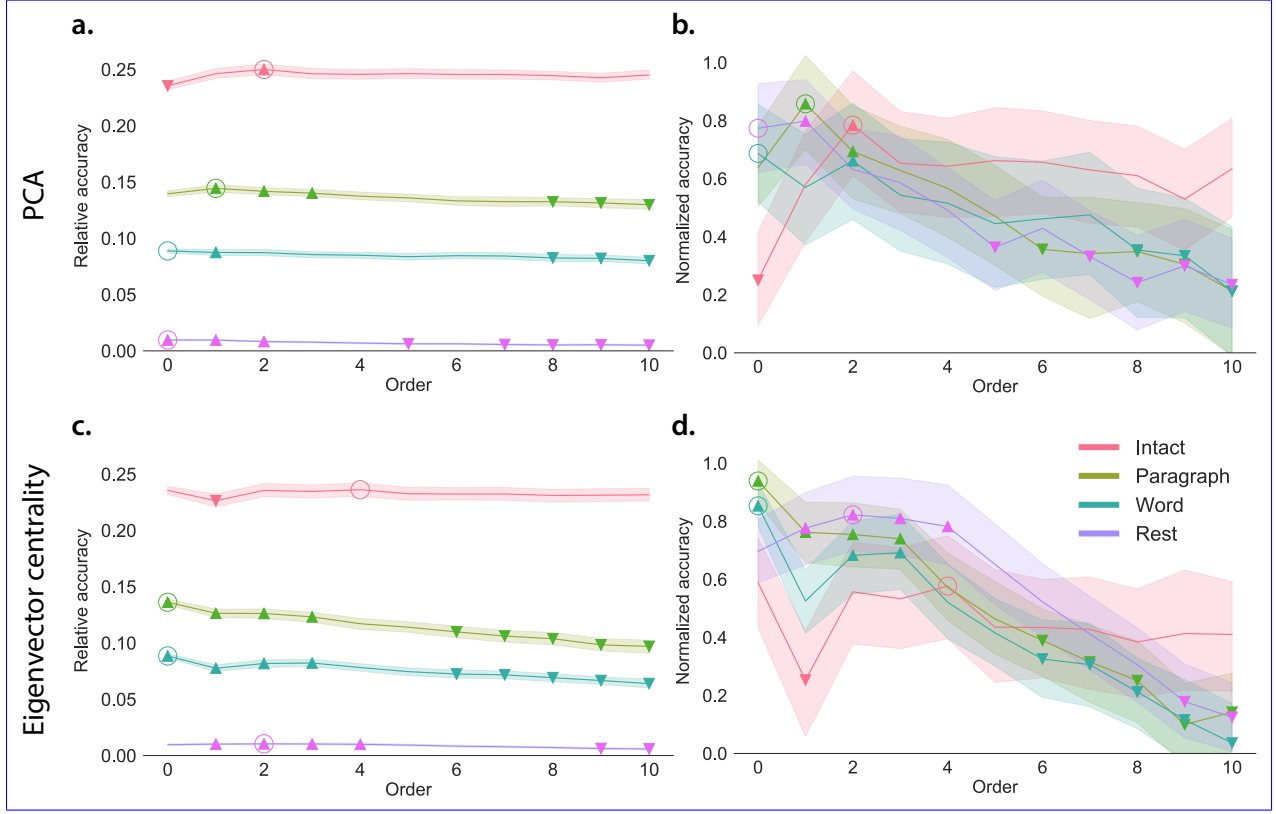


Figure 4: **Across-participant timepoint decoding accuracy varies with correlation order and cognitive engagement.** **a. Decoding accuracy as a function of order: PCA.** Order (x-axis) refers to the maximum order of dynamic correlations that were available to the classifiers (see *Feature weighting and testing*). The reported across-participant decoding accuracies are averaged over all kernel shapes and widths (see *Identifying robust decoding results*). The *y*-values are displayed relative to chance accuracy (intact: $\frac{1}{300}$; paragraph: $\frac{1}{272}$; word: $\frac{1}{300}$; rest: $\frac{1}{400}$). The error ribbons denote 95% confidence intervals across cross-validation folds (i.e., random assignments of participants to the training and test sets). The colors denote the experimental condition. Arrows denote sets of features that yielded reliably higher (upwards facing) or lower (downward facing) decoding accuracy than the mean of all other features (via a two-tailed test, thresholded at $p < 0.05$). Figure 5 displays additional comparisons between the decoding accuracies achieved using different sets of neural features. The circled values represent the maximum decoding accuracy within each experimental condition. **b. Normalized timepoint decoding accuracy as a function of order: PCA.** This panel displays the same results as Panel a, but here each curve has been normalized to have a maximum value of 1 and a minimum value of 0 (including the upper and lower bounds of the respective 95% confidence intervals). Panels a and b used PCA to project each high-dimensional pattern of dynamic correlations onto a lower-dimensional space. **c. Timepoint decoding accuracy as a function of order: eigenvector centrality.** This panel is in the same format as Panel a, but here eigenvector centrality has been used to project the high-dimensional patterns of dynamic correlations onto a lower-dimensional space. **d. Normalized timepoint decoding accuracy as a function of order: eigenvector centrality.** This panel is in the same format as Panel b, but here eigenvector centrality has been used to project the high-dimensional patterns of dynamic correlations onto a lower-dimensional space.

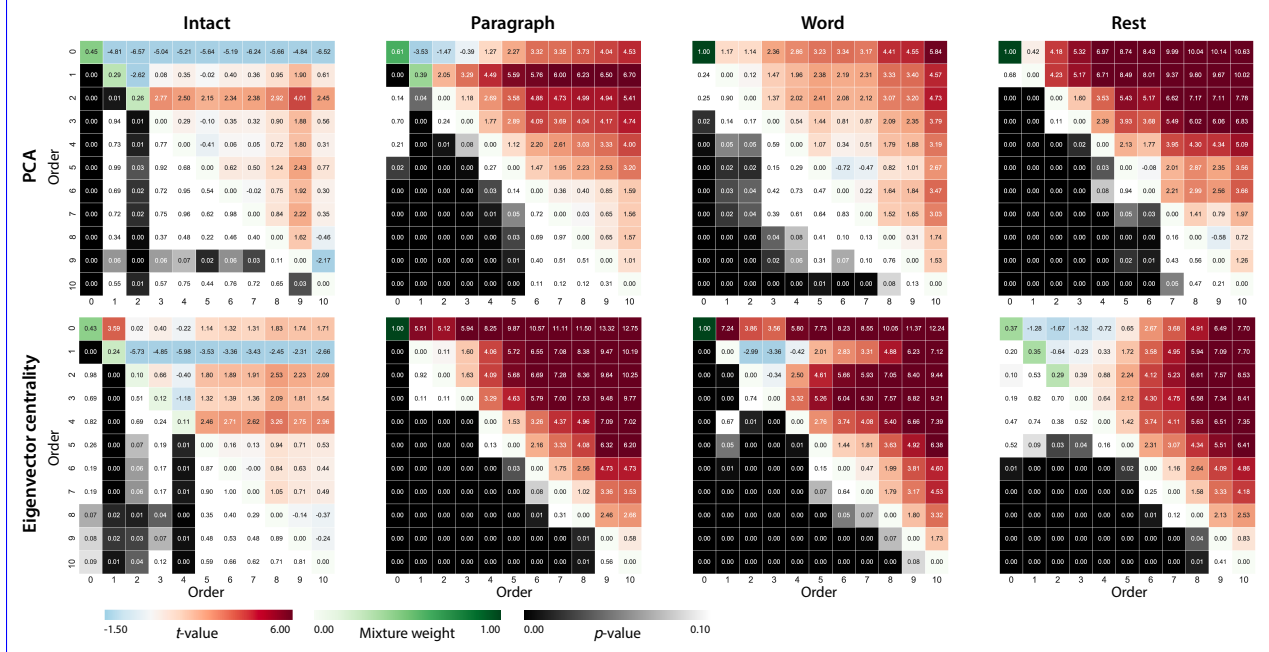


Figure 5: **Statistical summary of decoding accuracies for different neural features.** Each column of matrices displays decoding results for one experimental condition (intact, paragraph, word, and rest). We considered dynamic activity patterns (order 0) and dynamic correlations at different orders (order > 0). We used two-tailed t -tests to compare the distributions of decoding accuracies obtained using each pair of features. The distributions for each feature reflect the set of average decoding accuracies (across all kernel parameters), obtained for each random assignment of training and test groups. In the upper triangles of each matrix, warmer colors (positive t -values) indicate that the neural feature indicated in the given row yielded higher accuracy than the feature indicated in the given column. Cooler colors (negative t -values) indicate that the feature in the given row yielded lower decoding accuracy than the feature in the given column. The lower triangles of each map denote the corresponding p -values for the t -tests. The diagonal entries display the relative average optimized weight given to each type of feature, in a decoder that included all feature types (see *Feature weighting and testing*).

correlation matrices (Fig. 4a,b). The second set of analyses characterized correlations in dynamics of each feature's eigenvector centrality, but did not preserve the underlying activity dynamics (Fig. 4c,d). Both sets of temporal decoding analyses yielded qualitatively similar results for the auditory (non-rest) conditions of the experiment (Fig. 4: pink, green, and teal lines; Fig. 5: three leftmost columns). The highest decoding accuracy for participants who listened to the intact (unscrambled) story was achieved using high-order dynamic correlations (PCA: second-order; eigenvector-centrality: fourth-order). Scrambled versions of the story were best decoded by lower-order correlations (PCA/paragraph: first-order; PCA/word: order zero; eigenvector centrality/paragraph: order zero; eigenvector centrality/word: order zero). The two sets of analyses yielded different decoding results on resting state data (Fig. 4: purple lines; Fig. 5: rightmost column). We note that while the resting state times could be decoded reliably, the accuracies were only very slightly above chance. We speculate that the decoders might have picked up on attentional

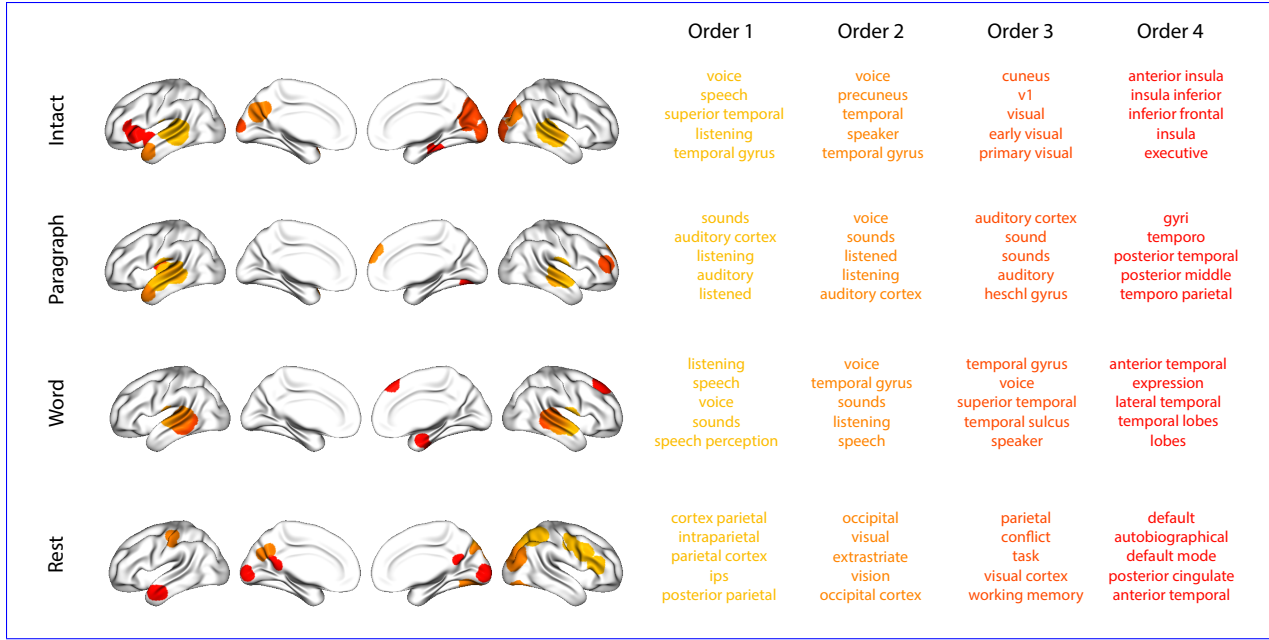


Figure 6: **Top terms associated with the endpoints of the strongest correlations.** Each color corresponds to one order of inter-subject functional correlations. To calculate the dynamic correlations, eigenvector centrality has been used to project the high-dimensional patterns of dynamic correlations onto a lower-dimensional space at each previous order, which allows us to map the brain regions at each order by retaining the features of the original space. The inflated brain plots display the locations of the endpoints of the 10 strongest (absolute value) correlations at each order, thresholded at 0.999, and projected onto the cortical surface (Combrisson et al., 2019). The lists of terms on the right display the top five Neurosynth terms (Rubin et al., 2017) decoded from the corresponding brain maps for each order. Each row displays data from a different experimental condition. Additional maps and their corresponding Neurosynth terms may be found in the *Supplementary materials* (intact: Fig. S1; paragraph: Fig. S2; word: Fig. S3; rest: Fig. S4).

193 drift, boredom, or tiredness; we hypothesize that these all increased throughout the resting state scan.
 194 The decoders might be picking up on aspects of these loosely defined cognitive states that are common
 195 across individuals. The PCA-based approach achieved the highest resting state decoding accuracy using
 196 order zero features (non-correlational, activation-based), whereas the eigenvector centrality-based approach
 197 achieved the highest resting state decoding accuracy using second-order correlations. Taken together, these
 198 analyses indicate that high-level cognitive processing (while listening to the intact story) is reflected in
 199 the dynamics of high-order correlations in brain activity, whereas lower-level cognitive processing (while
 200 listening to scrambled versions of the story that lack rich meaning) is reflected in the dynamics of lower-order
 201 correlations and non-correlational activity dynamics. Further, these patterns are associated both with the
 202 underlying activity patterns (characterized using PCA) and also with the changing relative positions that
 203 different brain areas occupy in their associated networks (characterized using eigenvector centrality).
 204 Having established that patterns of high-order correlations are informative to decoders, we next wondered
 205 which specific networks of brain regions contributed most to these patterns. As a representative example,

206 we selected the kernel parameters that yielded decoding accuracies that best matched the average accuracies
207 across all of the kernel parameters we examined. Using Figure 4c as a template, the best-matching kernel
208 was a Laplace kernel with a width of 50 (Fig. 9d). We used this kernel to compute a single K by K n^{th} -order
209 DISFC matrix for each experimental condition. We then used Neurosynth (Rubin et al., 2017) to compute
210 the terms most highly associated with the most strongly correlated pairs of regions in each of these matrices
211 (Fig. 6; see *Reverse inference*).

212 For all of the story listening conditions (intact, paragraph, and word), we found that first- and second-order
213 correlations were most strongly associated with auditory and speech processing areas. During intact story
214 listening, third-order correlations reflected integration with visual areas, and fourth-order correlations
215 reflected integration with areas associated with high-level cognition and cognitive control, such as the
216 ventrolateral prefrontal cortex. However, during listening to temporally scrambled stories, these higher-order
217 correlations instead involved interactions with additional regions associated with speech and semantic
218 processing. By contrast, we found a much different set of patterns in the resting state data. First-order
219 resting state correlations were most strongly associated with regions involved in counting and numerical
220 understanding. Second-order resting state correlations were strongest in visual areas; third-order correlations
221 were strongest in task-positive areas; and fourth-order correlations were strongest in regions associated with
222 autobiographical and episodic memory. We carried out analogous analyses to create maps (and decode the
223 top associated Neurosynth terms) for up to fifteenth-order correlations (Figs. S1, S2, S3, and S4). Of note,
224 examining fifteenth-order correlations between 700 nodes using conventional methods would have required
225 storing roughly $\frac{700^{2 \times 15}}{2} \approx 1.13 \times 10^{85}$ floating point numbers—assuming single-precision (32 bits each), this
226 would require roughly 32 times as many bits as there are molecules in the known universe! Although these
227 fifteenth-order correlations do appear (visually) to have some well-formed structure, we provide this latter
228 example primarily as a demonstration of the efficiency and scalability of our approach.

229 Discussion

230 We tested the hypothesis that high-level cognition is reflected in high-order brain network dynamics (e.g.,
231 see Reimann et al., 2017; Solomon et al., 2019). We examined high-order network dynamics in functional
232 neuroimaging data collected during a story listening experiment. When participants listened to an auditory
233 recording of the story, participants exhibited similar high-order brain network dynamics. By contrast,
234 when participants instead listened to temporally scrambled recordings of the story, only lower-order brain
235 network dynamics were similar across participants. Our results indicate that higher orders of network
236 interactions support higher-level aspects of cognitive processing (Fig. 7).

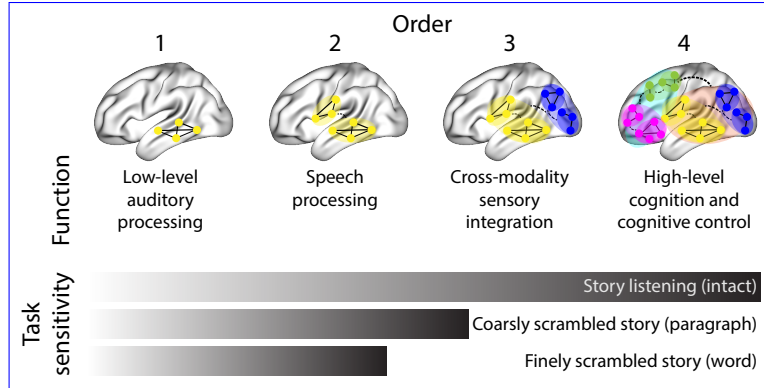


Figure 7: **Proposed high-order network dynamics underlying high-level cognition during story listening.** Schematic depicts higher orders of network interactions supporting higher-level aspects of cognitive processing. When tasks evoke richer, deeper, and/or higher-level processing, this is reflected in higher-order network interactions.

237 The notion that cognition is reflected in (and possibly mediated by) patterns of first-order network
 238 dynamics has been suggested by or proposed in myriad empirical studies and reviews (e.g., Chang &
 239 Glover, 2010; Demertzi et al., 2019; Fong et al., 2019; Gonzalez-Castillo et al., 2019; Liégeois et al., 2019; Lurie
 240 et al., 2018; Manning et al., 2018; Park et al., 2018; Preti et al., 2017; Roy et al., 2019; Turk-Browne, 2013;
 241 Zou et al., 2019). Our study extends this line of work by finding cognitively relevant *higher-order* network
 242 dynamics that reflect ongoing cognition. Our findings complement other work that uses graph theory and
 243 topology to characterize how brain networks reconfigure during cognition (e.g., Bassett et al., 2006; Betzel
 244 et al., 2019; McIntosh & Jirsa, 2019; Reimann et al., 2017; Sizemore et al., 2018; Toker & Sommer, 2019; Zheng
 245 et al., 2019).

246 An open question not addressed by our study pertains to how different structures integrate incoming
 247 information with different time constants. For example, one line of work suggests that the cortical surface
 248 comprises a structured map such that nearby brain structures process incoming information at similar
 249 timescales. Low-level sensory areas integrate information relatively quickly, whereas higher-level regions
 250 integrate information relatively slowly (Baldassano et al., 2017; Chien & Honey, 2019; Hasson et al.,
 251 2015, 2008; Honey et al., 2012; Lerner et al., 2014, 2011). A similar hierarchy appears to play a role in
 252 predicting future events (C. S. Lee et al., 2020). Other related work in human and mouse brains indicates
 253 that the temporal response profile of a given brain structure may relate to how strongly connected that
 254 structure is with other brain areas (Fallon et al., 2019). Further study is needed to understand the role of
 255 temporal integration at different scales of network interaction, and across different anatomical structures.
 256 Importantly, our analyses do not speak to the physiological basis of higher-order dynamics, and could reflect
 257 nonlinearities, chaotic patterns, non-stationarities, or multistability, etc. However, our decoding analyses

258 do indicate that higher-order dynamics are consistent across individuals, and therefore unlikely to be driven
259 by non-stimulus-driven dynamics which are unlikely to be similar across individuals.

260 Another potential limitation of our approach relates to recent work suggesting that the brain undergoes
261 rapid state changes, for example across event boundaries (e.g., Baldassano et al., 2017). Shappell et al. (2019)
262 used hidden semi-Markov models to estimate state-specific network dynamics (also see Vidaurre et al.,
263 2018). Our general approach might be extended by considering putative state transitions. For example,
264 rather than weighting all timepoints using a similar kernel (Eqn. 4), the kernel function could adapt on a
265 timepoint-by-timepoint basis such that only timepoints determined to be in the same “state” were given
266 non-zero weight.

267 Identifying high-order network dynamics associated with high-level cognition required several important
268 methods advances. First, we used kernel-based dynamic correlations to extend the notion of (static)
269 inter-subject functional connectivity (Simony et al., 2016) to a dynamic measure of inter-subject functional
270 connectivity (DISFC) that does not rely on sliding windows (e.g., as in Manning et al., 2018), and that may
271 be computed at individual timepoints. This allowed us to precisely characterize stimulus-evoked network
272 dynamics that were similar across individuals. Second, we developed a computational framework for
273 efficiently and scalably estimating high-order dynamic correlations. Our approach uses dimensionality
274 reduction algorithms and graph measures to obtain low-dimensional embeddings of patterns of network
275 dynamics. Third, we developed an analysis framework for identifying robust decoding results by carrying
276 out our analyses using a range of parameter values and then identifying which results were robust to specific
277 parameter choices.

278 **Concluding remarks**

279 Methods for characterizing the dynamics of high-order correlations in neural data provide a window into the
280 neural basis of cognition. By showing that high-level cognition is reflected in high-order network dynamics,
281 we have elucidated the next step on the path towards understanding the neural basis of cognition.

282 **Methods**

283 Our general approach to efficiently estimating high-order dynamic correlations comprises four general
284 steps (Fig. 8). First, we derive a kernel-based approach to computing dynamic pairwise correlations in
285 a T (timepoints) by K (features) multivariate timeseries, \mathbf{X}_0 . This yields a T by $O(K^2)$ matrix of dynamic
286 correlations, \mathbf{Y}_1 , where each row comprises the upper triangle and diagonal of the correlation matrix at

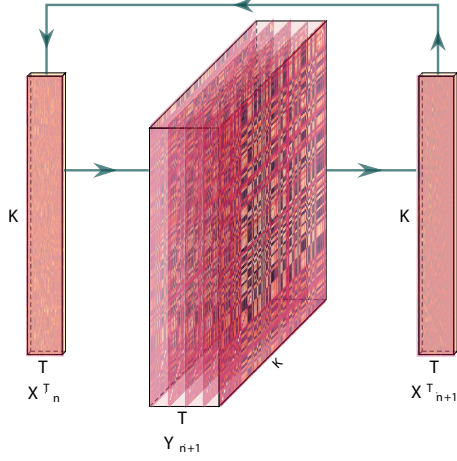


Figure 8: **Estimating dynamic high-order correlations.** Given a T by K matrix of multivariate timeseries data, \mathbf{X}_n (where $n \in \mathbb{N}, n \geq 0$), we use Equation 4 to compute a timeseries of K by K correlation matrices, \mathbf{Y}_{n+1} . We then approximate \mathbf{Y}_{n+1} with the T by K matrix \mathbf{X}_{n+1} . This process may be repeated to scalably estimate iteratively higher-order correlations in the data. Note that the transposes of \mathbf{X}_n and \mathbf{X}_{n+1} are displayed in the figure for compactness.

287 a single timepoint, reshaped into a row vector (this reshaped vector is $(\frac{K^2-K}{2} + K)$ -dimensional). Second,
 288 we apply a dimensionality reduction step to project the matrix of dynamic correlations back onto a K -
 289 dimensional space. This yields a T by K matrix, \mathbf{X}_1 , that reflects an approximation of the dynamic correlations
 290 reflected in the original data. Third, we use repeated applications of the kernel-based dynamic correlation
 291 step to \mathbf{X}_n and the dimensionality reduction step to the resulting \mathbf{Y}_{n+1} to estimate high-order dynamic
 292 correlations. Each application of these steps to a T by K time series \mathbf{X}_n yields a T by K matrix, \mathbf{X}_{n+1} , that
 293 reflects the dynamic correlations between the columns of \mathbf{X}_n . In this way, we refer to n as the *order* of the
 294 timeseries, where \mathbf{X}_0 (order 0) denotes the original data and \mathbf{X}_n denotes (approximated) n^{th} -order dynamic
 295 correlations between the columns of \mathbf{X}_0 . Finally, we use a cross-validation-based decoding approach to
 296 evaluate how well information contained in a given order (or weighted mixture of orders) may be used
 297 to decode relevant cognitive states. If including a given \mathbf{X}_n in the feature set yields higher classification
 298 accuracy on held-out data, we interpret this as evidence that the given cognitive states are reflected in
 299 patterns of n^{th} -order correlations.

300 All of the code used to produce the figures and results in this manuscript, along with links to the
 301 corresponding datasets, may be found at github.com/ContextLab/timecorr-paper. In addition, we have
 302 released a Python toolbox for computing dynamic high-order correlations in timeseries data; our toolbox
 303 may be found at timecorr.readthedocs.io.

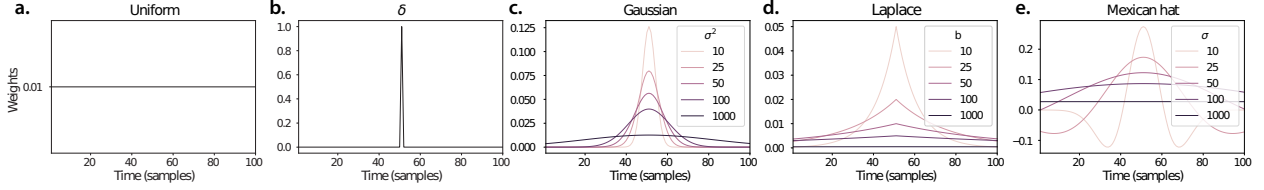


Figure 9: Examples of kernel functions. Each panel displays per-timepoint weights for a kernel centered at $t = 50$, evaluated at 100 timepoints ($\tau \in [1, \dots, 100]$). **a. Uniform kernel.** The weights are timepoint-invariant; observations at all timepoints are weighted equally, and do not change as a function of τ . This is a special case kernel function that reduces dynamic correlations to static correlations. **b. Dirac δ kernel.** Only the observation at timepoint t is given a non-zero weight (of 1). **c. Gaussian kernels.** Each kernel's weights fall off in time according to a Gaussian probability density function centered on time t . Weights derived using several different example width parameters (σ^2) are displayed. **d. Laplace kernels.** Each kernel's weights fall off in time according to a Laplace probability density function centered on time t . Weights derived using several different example width parameters (b) are displayed. **e. Mexican hat (Ricker wavelet) kernels.** Each kernel's weights fall off in time according to a Ricker wavelet centered on time t . This function highlights the *contrasts* between local versus surrounding activity patterns in estimating dynamic correlations. Weights derived using several different example width parameters (σ) are displayed.

304 Kernel-based approach for computing dynamic correlations

Given a T by K matrix of observations, \mathbf{X} , we can compute the (static) Pearson's correlation between any pair of columns, $\mathbf{X}(\cdot, i)$ and $\mathbf{X}(\cdot, j)$ using (Pearson, 1901):

$$\text{corr}(\mathbf{X}(\cdot, i), \mathbf{X}(\cdot, j)) = \frac{\sum_{t=1}^T (\mathbf{X}(t, i) - \bar{\mathbf{X}}(\cdot, i)) (\mathbf{X}(t, j) - \bar{\mathbf{X}}(\cdot, j))}{\sqrt{\sum_{t=1}^T \sigma_{\mathbf{X}(\cdot, i)}^2 \sigma_{\mathbf{X}(\cdot, j)}^2}}, \text{ where} \quad (1)$$

$$\bar{\mathbf{X}}(\cdot, k) = \frac{1}{T} \sum_{t=1}^T \mathbf{X}(t, k), \text{ and} \quad (2)$$

$$\sigma_{\mathbf{X}(\cdot, k)}^2 = \frac{1}{T} \sum_{t=1}^T (\mathbf{X}(t, k) - \bar{\mathbf{X}}(\cdot, k))^2 \quad (3)$$

- 305 We can generalize this formula to compute time-varying correlations by incorporating a *kernel function* that
 306 takes a time t as input, and returns how much the observed data at each timepoint $\tau \in [-\infty, \infty]$ contributes
 307 to the estimated instantaneous correlation at time t (Fig. 9; also see Allen et al., 2012, for a similar approach).

308

Given a kernel function $\kappa_t(\cdot)$ for timepoint t , evaluated at timepoints $\tau \in [1, \dots, T]$, we can update the

static correlation formula in Equation 1 to estimate the *instantaneous correlation* at timepoint t :

$$\text{timecorr}_{\kappa_t}(\mathbf{X}(\cdot, i), \mathbf{X}(\cdot, j)) = \frac{\sum_{\tau=1}^T (\mathbf{X}(\tau, i) - \tilde{\mathbf{X}}_{\kappa_t}(\cdot, i))(\mathbf{X}(\tau, j) - \tilde{\mathbf{X}}_{\kappa_t}(\cdot, j))}{\sqrt{\sum_{\tau=1}^T \tilde{\sigma}_{\kappa_t}^2(\mathbf{X}(\cdot, i)) \tilde{\sigma}_{\kappa_t}^2(\mathbf{X}(\cdot, j))}}, \text{ where} \quad (4)$$

$$\tilde{\mathbf{X}}_{\kappa_t}(\cdot, k) = \sum_{\tau=1}^T \kappa_t(\tau) \mathbf{X}(\tau, k), \quad (5)$$

$$\tilde{\sigma}_{\kappa_t}^2(\mathbf{X}(\cdot, k)) = \sum_{\tau=1}^T (\mathbf{X}(\tau, k) - \tilde{\mathbf{X}}_{\kappa_t}(\cdot, k))^2. \quad (6)$$

309 Here $\text{timecorr}_{\kappa_t}(\mathbf{X}(\cdot, i), \mathbf{X}(\cdot, j))$ reflects the correlation at time t between columns i and j of \mathbf{X} , estimated using
 310 the kernel κ_t . We evaluate Equation 4 in turn for each pair of columns in \mathbf{X} and for kernels centered on each
 311 timepoint in the timeseries, respectively, to obtain a T by K by K timeseries of dynamic correlations, \mathbf{Y} . For
 312 convenience, we then reshape the upper triangles and diagonals of each timepoint's symmetric correlation
 313 matrix into a row vector to obtain an equivalent T by $(\frac{K^2-K}{2} + K)$ matrix.

314 **Dynamic inter-subject functional connectivity (DISFC)**

Equation 4 provides a means of taking a single observation matrix, \mathbf{X}_n and estimating the dynamic correlations from moment to moment, \mathbf{Y}_{n+1} . Suppose that one has access to a set of multiple observation matrices that reflect the same phenomenon. For example, one might collect neuroimaging data from several experimental participants, as each participant performs the same task (or sequence of tasks). Let $\mathbf{X}_n^1, \mathbf{X}_n^2, \dots, \mathbf{X}_n^P$ reflect the T by K observation matrices ($n = 0$) or reduced correlation matrices ($n > 0$) for each of P participants in an experiment. We can use *inter-subject functional connectivity* (ISFC; Simony & Chang, 2020; Simony et al., 2016) to compute the stimulus-driven correlations reflected in the multi-participant dataset at a given timepoint t using:

$$\tilde{\mathbf{C}}(t) = M \left(R \left(\frac{1}{2P} \sum_{p=1}^P Z(\mathbf{Y}_{n+1}^p(t))^\top + Z(\mathbf{Y}_{n+1}^p(t)) \right) \right), \quad (7)$$

where M extracts and vectorizes the upper triangle and diagonal of a symmetric matrix, Z is the Fisher z -transformation (Zar, 2010):

$$Z(r) = \frac{\log(1+r) - \log(1-r)}{2}, \quad (8)$$

R is the inverse of Z :

$$R(z) = \frac{\exp(2z - 1)}{\exp(2z + 1)}, \quad (9)$$

and $\mathbf{Y}_{n+1}^p(t)$ denotes the correlation matrix at timepoint t (Eqn. 4) between each column of \mathbf{X}_n^p and each column of the average \mathbf{X}_n from all *other* participants, $\bar{\mathbf{X}}_n^{\setminus p}$:

$$\bar{\mathbf{X}}_n^{\setminus p} = \frac{1}{P-1} \sum_{q \in \setminus p} \mathbf{X}_n^q, \quad (10)$$

315 where $\setminus p$ denotes the set of all participants other than participant p . In this way, the T by $\binom{K^2-K}{2} + K$ DISFC
 316 matrix $\bar{\mathbf{C}}$ provides a time-varying extension of the ISFC approach developed by Simony et al. (2016).

317 Low-dimensional representations of dynamic correlations

318 Given a T by $\binom{K^2-K}{2} + K$ matrix of n^{th} -order dynamic correlations, \mathbf{Y}_n , we propose two general approaches
 319 to computing a T by K low-dimensional representation of those correlations, \mathbf{X}_n . The first approach uses
 320 dimensionality reduction algorithms to project \mathbf{Y}_n onto a K -dimensional space. The second approach uses
 321 graph measures to characterize the relative positions of each feature ($k \in [1, \dots, K]$) in the network defined
 322 by the correlation matrix at each timepoint.

323 Dimensionality reduction-based approaches to computing \mathbf{X}_n

324 The modern toolkit of dimensionality reduction algorithms include Principal Components Analysis (PCA;
 325 Pearson, 1901), Probabilistic PCA (PPCA; Tipping & Bishop, 1999), Exploratory Factor Analysis (EFA;
 326 Spearman, 1904), Independent Components Analysis (ICA; Comon et al., 1991; Jutten & Herault, 1991),
 327 t -Stochastic Neighbor Embedding (t -SNE; van der Maaten & Hinton, 2008), Uniform Manifold Approximation and Projection (UMAP; McInnes et al., 2018), non-negative matrix factorization (NMF; D. D. Lee
 328 & Seung, 1999), Topographic Factor Analysis (TFA; Manning et al., 2014), Hierarchical Topographic Factor analysis (HTFA; Manning et al., 2018), Topographic Latent Source Analysis (TLSA; Gershman et al.,
 329 2011), dictionary learning (J. Mairal et al., 2009; J. B. Mairal et al., 2009), and deep auto-encoders (Hinton
 330 & Salakhutdinov, 2006), among others. While complete characterizations of each of these algorithms is
 331 beyond the scope of the present manuscript, the general intuition driving these approaches is to compute
 332 the T by K matrix, \mathbf{X} , that is closest to the original T by J matrix, \mathbf{Y} , where (typically) $K \ll J$. The different
 333 approaches place different constraints on what properties \mathbf{X} must satisfy and which aspects of the data are
 334 compared (and how) in order to optimize how well \mathbf{X} approximates \mathbf{Y} .

337 Applying dimensionality reduction algorithms to \mathbf{Y} yields an \mathbf{X} whose columns reflect weighted com-
338 binations (or nonlinear transformations) of the original columns of \mathbf{Y} . This has two main consequences.
339 First, with each repeated dimensionality reduction, the resulting \mathbf{X}_n has lower and lower fidelity (with
340 respect to what the “true” \mathbf{Y}_n might have looked like without using dimensionality reduction to maintain
341 **scalability****tractability**). In other words, computing \mathbf{X}_n is a lossy operation. Second, whereas each column
342 of \mathbf{Y}_n may be mapped directly onto specific pairs of columns of \mathbf{X}_{n-1} , the columns of \mathbf{X}_n reflect weighted
343 combinations and/or nonlinear transformations of the columns of \mathbf{Y}_n . Many dimensionality reduction algo-
344 rithms are invertible (or approximately invertible). However, attempting to map a given \mathbf{X}_n back onto the
345 original feature space of \mathbf{X}_0 will usually require $O(TK^{2n})$ space and therefore becomes intractable as n or K
346 grow large.

347 **Graph measure approaches to computing \mathbf{X}_n**

348 The above dimensionality reduction approaches to approximating a given \mathbf{Y}_n with a lower-dimensional
349 \mathbf{X}_n preserve a (potentially recombined and transformed) mapping back to the original data in \mathbf{X}_0 . We also
350 explore graph measures that instead characterize each feature’s relative *position* in the broader network of
351 interactions and connections. To illustrate the distinction between the two general approaches we explore,
352 suppose a network comprises nodes A ~~-and~~ B , ~~and~~ C along with several other nodes. If A and B exhibit
353 uncorrelated activity patterns, ~~then by definition~~ the functional connection (correlation) between them will
354 be ~~(by definition)~~ close to 0. However, if A and B each interact with ~~C~~ other nodes in similar ways, we might
355 attempt to capture those similarities ~~using a measure that reflects how between A’s and B interact with other~~
356 ~~’s interactions with those other~~ members of the network.

357 In general, graph measures take as input a matrix of interactions (e.g., using the above notation, a K
358 by K correlation matrix or binarized correlation matrix reconstituted from a single timepoint’s row of \mathbf{Y}),
359 and return as output a set of K measures describing how each node (feature) sits within that correlation
360 matrix with respect to the rest of the population. Widely used measures include betweenness centrality (the
361 proportion of shortest paths between each pair of nodes in the population that involves the given node
362 in question; e.g., Barthélemy, 2004; Freeman, 1977; Geisberger et al., 2008; Newman, 2005; Opsahl et al.,
363 2010); diversity and dissimilarity (characterizations of how differently connected a given node is from others
364 in the population; e.g., Lin, 2009; Rao, 1982; Ricotta & Szeidl, 2006); eigenvector centrality and pagerank
365 centrality (measures of how influential a given node is within the broader network; e.g., Bonacich, 2007;
366 Halu et al., 2013; Lohmann et al., 2010; Newman, 2008); transfer entropy and flow coefficients (a measure of
367 how much information is flowing from a given node to other nodes in the network; e.g., Honey et al., 2007;

368 Schreiber, 2000); k -coreness centrality (a measure of the connectivity of a node within its local subgraph; e.g.,
369 Alvarez-Hamelin et al., 2005; Christakis & Fowler, 2010); within-module degree (a measure of how many
370 connections a node has to its close neighbors in the network; e.g., Rubinov & Sporns, 2010); participation
371 coefficient (a measure of the diversity of a node's connections to different subgraphs in the network; e.g.,
372 Rubinov & Sporns, 2010); and subgraph centrality (a measure of a node's participation in all of the network's
373 subgraphs; e.g., Estrada & Rodríguez-Velázquez, 2005); among others.

374 For a given graph measure, $\eta : \mathbb{R}^{K \times K} \rightarrow \mathbb{R}^K$, we can use η to transform each row of \mathbf{Y}_n in a way that
375 characterizes the corresponding graph properties of each column. This results in a new T by K matrix,
376 \mathbf{X}_n , that reflects how the features reflected in the columns of \mathbf{X}_{n-1} participate in the network during each
377 timepoint (row).

378 **Dynamic higher-order correlations**

379 Because \mathbf{X}_n has the same shape as the original data \mathbf{X}_0 , approximating \mathbf{Y}_n with a lower-dimensional \mathbf{X}_n enables
380 us to estimate high-order dynamic correlations in a scalable way. Given a T by K input matrix, the output
381 of Equation 4 requires $O(TK^2)$ space to store. Repeated applications of Equation 4 (i.e., computing dynamic
382 correlations between the columns of the outputted dynamic correlation matrix) each require exponentially
383 more space; in general the n^{th} -order dynamic correlations of a T by K timeseries occupies $\mathcal{O}(TK^{2n})$ $\mathcal{O}(TK^{2^n})$
384 space. However, when we approximate or summarize the output of Equation 4 with a T by K matrix (as
385 described above), it becomes feasible to compute even very high-order correlations in high-dimensional
386 data. Specifically, approximating the n^{th} -order dynamic correlations of a T by K timeseries requires only
387 $O(TK^2)$ additional space— the same as would be required to compute first-order dynamic correlations. In
388 other words, the space required to store $n + 1$ multivariate timeseries reflecting up to n^{th} order correlations
389 in the original data scales linearly with n using our approach (Fig. 8).

390 **Data**

391 We examined two types of data: synthetic data and human functional neuroimaging data. We constructed
392 and leveraged the synthetic data to evaluate our general approach (for a related validation approach see
393 Thompson et al., 2018). Specifically, we tested how well Equation 4 could be used to recover known dynamic
394 correlations using different choices of kernel (κ ; Fig. 9), for each of several synthetic datasets that exhibited
395 different temporal properties. We also simulated higher-order correlations and tested how well Equation 4
396 could recover these correlations using the best kernel from the previous synthetic data analyses. We then
397 applied our approach to a functional neuroimaging dataset to test the hypothesis that ongoing cognitive

398 processing is reflected in high-order dynamic correlations. We used an across-participant classification test
 399 to estimate whether dynamic correlations of different orders contain information about which timepoint in
 400 a story participants were listening to.

401 **Synthetic data: simulating dynamic first-order correlations**

402 We constructed a total of 40 different multivariate timeseries, collectively reflecting a total of 4 qualitatively
 403 different patterns of dynamic first-order correlations (i.e., 10 datasets reflecting each type of dynamic pat-
 404 tern). Each timeseries comprised 50 features (dimensions) that varied over 300 timepoints. The observations
 405 at each timepoint were drawn from a zero-mean multivariate Gaussian distribution with a covariance matrix
 406 defined for each timepoint as described below. We drew the observations at each timepoint independently
 407 from the draws at all other timepoints; in other words, for each observation $s_t \sim \mathcal{N}(\mathbf{0}, \Sigma_t)$ at timepoint t ,
 408 $p(s_t) = p(s_t | s_{\setminus t})$.

Constant. We generated data with stable underlying correlations to evaluate how Equation 4 characterized correlation “dynamics” when the ground truth correlations were static. We constructed 10 multivariate timeseries whose observations were each drawn from a single (stable) Gaussian distribution. For each dataset (indexed by m), we constructed a random covariance matrix, Σ_m :

$$\underline{\Sigma_m = CC^\top}, \text{ where} \quad (11)$$

$$\underline{C(i, j) \sim N(0, 1)} \underline{\Sigma_m = CC^\top}, \text{ where, and where} \quad (12)$$

409 $i, j \in [1, 2, \dots, 50]$. In other words, all of the observations (for each of the 300 timepoints) within each dataset
 410 were drawn from a multivariate Gaussian distribution with the same covariance matrix, and the 10 datasets
 411 each used a different covariance matrix.

412 **Random.** We generated a second set of 10 synthetic datasets whose observations at each timepoint were
 413 drawn from a Gaussian distribution with a new randomly constructed (using Eqn. 11) covariance matrix.
 414 Because each timepoint’s covariance matrix was drawn independently from the covariance matrices for all
 415 other timepoints, these datasets provided a test of reconstruction accuracy in the absence of any meaningful
 416 underlying temporal structure in the dynamic correlations underlying the data.

Ramping. We generated a third set of 10 synthetic datasets whose underlying correlations changed gradu-
 ally over time. For each dataset, we constructed two *anchor* covariance matrices using Equation 11, Σ_{start}

and Σ_{end} . For each of the 300 timepoints in each dataset, we drew the observations from a multivariate Gaussian distribution whose covariance matrix at each timepoint $t \in [0, \dots, 299]$ was given by

$$\Sigma_t = \left(1 - \frac{t}{299}\right)\Sigma_{\text{start}} + \frac{t}{299}\Sigma_{\text{end}}. \quad (13)$$

417 The gradually changing correlations underlying these datasets allow us to evaluate the recovery of dynamic
 418 correlations when each timepoint's correlation matrix is unique (as in the random datasets), but where the
 419 correlation dynamics are structured [and exhibit first-order autocorrelations \(as in the constant datasets\)](#).

420 **Event.** We generated a fourth set of 10 synthetic datasets whose underlying correlation matrices exhibited
 421 prolonged intervals of stability, interspersed with abrupt changes. For each dataset, we used Equation 11
 422 to generate 5 random covariance matrices. We constructed a timeseries where each set of 60 consecutive
 423 samples was drawn from a Gaussian with the same covariance matrix. These datasets were intended to
 424 simulate a system that [undergoes exhibits periods of stability punctuated by](#) occasional abrupt state changes.

425 [**Synthetic data: simulating dynamic high-order correlations**](#)

426 [We developed an iterative procedure for constructing timeseries data that exhibits known dynamic high-order](#)
 427 [correlations. The procedure builds on our approach to generating dynamic first-order correlations. Essentially,](#)
 428 [once we generate a timeseries with known first-order correlations, we can use the known first-order](#)
 429 [correlations as a template to generate a new timeseries of second-order correlations. In turn, we can](#)
 430 [generate a timeseries of third-order correlations from the second-order correlations, and so on. In general,](#)
 431 [we can generate order \$n\$ correlations given a timeseries of order \$n - 1\$ correlations, for any \$n > 1\$. Finally,](#)
 432 [given the order \$n\$ timeseries, we can reverse the preceding process to generate an order \$n - 1\$ timeseries, an](#)
 433 [order \$n - 2\$ order timeseries, and so on, until we obtain an order 0 timeseries of simulated data that reflects](#)
 434 [the chosen high-order dynamics.](#)

The central mathematical operations in our procedure are two functions, $\text{vec}(\cdot)$ and $\text{mat}(\cdot)$. The $\text{vec}(\cdot)$ function takes as input a $K \times K$ symmetric matrix and returns as output a $(\frac{K^2-K}{2} + K)$ -dimensional column vector containing the entries in the upper triangle and diagonal. The $\text{mat}(\cdot)$ function inverts $\text{vec}(\cdot)$ by taking as input a $(\frac{K^2-K}{2} + K)$ -dimensional column vector and returning a $K \times K$ symmetric matrix as output. We can then generate an order n correlation matrix (for one timepoint, t) from an order $n - 1$ template (from the same timepoint) as follows:

$$\Sigma_n(t) = \text{mat}(\text{vec}(\Sigma_{n-1}(t)) \otimes \text{vec}(\Sigma_{n-1}(t))^\top). \quad (14)$$

Given a timeseries of order n correlation matrices, we can draw an order $n - 1$ correlation matrix for each timepoint t using

$$\sigma_{n-1}(t) \sim \mathcal{N}(\mathbf{0}, \Sigma_n(t)) \quad (15)$$

$$\Sigma_{n-1}(t) = \text{mat}(\sigma_{n-1}(t)). \quad (16)$$

435 We can then use repeated applications of Equations 15 and 16 in order to obtain a synthetic dataset.
436 When the template first-order correlations are constructed to exhibit different temporal profiles (e.g.,
437 using the constant, random, ramping, and event procedures described above), the resulting high-order
438 correlations and synthetic data will exhibit the same category of temporal profile.
439 Following our approach to generating synthetic data exhibiting known first-order correlations, we
440 constructed a total of 40 additional multivariate timeseries, collectively reflecting a total of 4 qualitatively
441 different patterns of dynamic correlations (i.e., 10 datasets reflecting each type of dynamic pattern: constant,
442 random, ramping, and event).

443 Functional neuroimaging data collected during story listening

444 We examined an fMRI dataset collected by Simony et al. (2016) that the authors have made publicly available
445 at arks.princeton.edu/ark:/88435/dsp015d86p269k. The dataset comprises neuroimaging data collected as
446 participants listened to an audio recording of a story (intact condition; 36 participants), listened to temporally
447 scrambled recordings of the same story (17 participants in the paragraph-scrambled condition listened to
448 the paragraphs in a randomized order and 36 in the word-scrambled condition listened to the words in a
449 randomized order), or lay resting with their eyes open in the scanner (rest condition; 36 participants). Full
450 neuroimaging details may be found in the original paper for which the data were collected (Simony et al.,
451 2016).

452 **Hierarchical topographic factor analysis (HTFA).** Following our prior related work, we used HTFA (Manning et al., 2018) to derive a compact representation of the neuroimaging data. In brief, this approach approximates the timeseries of voxel activations (44,415 voxels) using a much smaller number of radial basis function (RBF) nodes (in this case, 700 nodes, as determined by an optimization procedure described by Manning et al., 2018). This provides a convenient representation for examining full-brain network dynamics. All of the analyses we carried out on the neuroimaging dataset were performed in this lower-dimensional space. In other words, each participant's data matrix, \mathbf{X}_0 , was a number-of-timepoints by 700 matrix of HTFA-derived factor weights (where the row and column labels were matched across participants). Code

460 for carrying out HTFA on fMRI data may be found as part of the BrainIAK toolbox (Capota et al., 2017),
461 which may be downloaded at brainiak.org.

462 Temporal decoding

463 We sought to identify neural patterns that reflected participants' ongoing cognitive processing of incoming
464 stimulus information. As reviewed by Simony et al. (2016), one way of homing in on these stimulus-driven
465 neural patterns is to compare activity patterns across individuals (e.g., using ISFC analyses). In particular,
466 neural patterns will be similar across individuals to the extent that the neural patterns under consideration
467 are stimulus-driven, and to the extent that the corresponding cognitive representations are reflected in
468 similar spatial patterns across people (also see Simony & Chang, 2020). Following this logic, we used an
469 across-participant temporal decoding test developed by Manning et al. (2018) to assess the degree to which
470 different neural patterns reflected ongoing stimulus-driven cognitive processing across people –(Fig. 10).
471 The approach entails using a subset of the data to train a classifier to decode stimulus timepoints (i.e.,
472 moments in the story participants listened to) from neural patterns. We use decoding (forward inference)
473 accuracy on held-out data, from held-out participants, as a proxy for the extent to which the inputted neural
474 patterns reflected stimulus-driven cognitive processing in a similar way across individuals.

475 Forward inference and decoding accuracy

476 We used an across-participant correlation-based classifier to decode which stimulus timepoint matched each
477 timepoint's neural pattern –(Fig. 10). We first divided the participants into two groups: a template group,
478 $\mathcal{G}_{\text{template}}$ –(i.e., training data), and a to-be-decoded group, $\mathcal{G}_{\text{decode}}$ –(i.e., test data). We used Equation 7 to
479 compute a DISFC matrix for each group ($\bar{\mathbf{C}}_{\text{template}}$ and $\bar{\mathbf{C}}_{\text{decode}}$, respectively). We then correlated the rows of
480 $\bar{\mathbf{C}}_{\text{template}}$ and $\bar{\mathbf{C}}_{\text{decode}}$ to form a number-of-timepoints by number-of-timepoints decoding matrix, Λ . In this
481 way, the rows of Λ reflected timepoints from the template group, while the columns reflected timepoints
482 from the to-be-decoded group. We used Λ to assign temporal labels to each row $\bar{\mathbf{C}}_{\text{decode}}$ using the row of
483 $\bar{\mathbf{C}}_{\text{template}}$ with which it was most highly correlated. We then repeated this decoding procedure, but using
484 $\mathcal{G}_{\text{decode}}$ as the template group and $\mathcal{G}_{\text{template}}$ as the to-be-decoded group. Given the true timepoint labels (for
485 each group), we defined the *decoding accuracy* as the average proportion of correctly decoded timepoints,
486 across both groups. We defined the *relative decoding accuracy* as the difference between the decoding accuracy
487 and chance accuracy (i.e., $\frac{1}{T}$).

488 **Feature weighting and testing**

489 We sought to examine which types of neural features (i.e., activations, first-order dynamic correlations, and
490 higher-order dynamic correlations) were informative to the temporal decoders. Using the notation above,
491 these features correspond to $\mathbf{X}_0, \mathbf{X}_1, \mathbf{X}_2, \mathbf{X}_3$, and so on.

492 One challenge to fairly evaluating high-order correlations is that if the kernel used in Equation 4 is
493 wider than a single timepoint, each repeated application of the equation will result in further temporal
494 blur. Because our primary assessment metric is temporal decoding accuracy, this unfairly biases against
495 detecting meaningful signal in higher-order correlations (relative to lower-order correlations). We attempted
496 to mitigate temporal blur in estimating each \mathbf{X}_n by using a Dirac δ function kernel (which places all of its
497 mass over a single timepoint; Fig. 9b, [10a](#)) to compute each lower-order correlation ($\mathbf{X}_1, \mathbf{X}_2, \dots, \mathbf{X}_{n-1}$). We
498 then used a new (potentially wider, as described below) kernel to compute \mathbf{X}_n from \mathbf{X}_{n-1} . In this way,
499 temporal blurring was applied only in the last step of computing \mathbf{X}_n . We note that, because each \mathbf{X}_n is a
500 low-dimensional representation of the corresponding \mathbf{Y}_n , the higher-order correlations we estimated reflect
501 true correlations in the data with lower-fidelity than estimates of lower-order correlations. Therefore, even
502 after correcting for temporal blurring, our approach is still biased against finding meaningful signal in
503 higher-order correlations.

504 After computing each $\mathbf{X}_1, \mathbf{X}_2, \dots, \mathbf{X}_{n-1}$ for each participant, we divided participants into two equally sized
505 groups (± 1 for odd numbers of participants): $\mathcal{G}_{\text{train}}$ and $\mathcal{G}_{\text{test}}$. We then further subdivided $\mathcal{G}_{\text{train}}$ into $\mathcal{G}_{\text{train}_1}$
506 and $\mathcal{G}_{\text{train}_2}$. We then computed Λ (temporal correlation) matrices for each type of neural feature, using $\mathcal{G}_{\text{train}_1}$
507 and $\mathcal{G}_{\text{train}_2}$. This resulted in $n + 1$ Λ matrices (one for the original timeseries of neural activations, and one
508 for each of n orders of dynamic correlations). Our objective was to find a set of weights for each of these
509 Λ matrices such that the weighted average of the $n + 1$ matrices yielded the highest decoding accuracy.
510 We used quasi-Newton gradient ascent (Nocedal & Wright, 2006), using decoding accuracy (for $\mathcal{G}_{\text{train}_1}$ and
511 $\mathcal{G}_{\text{train}_2}$) as the objective function to be maximized, to find an optimal set of training data-derived weights,
512 $\phi_{0,1,\dots,n}$, where $\sum_{i=0}^n \phi_i = 1$ and where $\phi_i \geq 0 \forall i \in [0, 1, \dots, n]$.

513 After estimating an optimal set of weights, we computed a new set of $n + 1$ Λ matrices correlating the
514 DISFC patterns from $\mathcal{G}_{\text{train}}$ and $\mathcal{G}_{\text{test}}$ at each timepoint. We use the resulting decoding accuracy of $\mathcal{G}_{\text{test}}$
515 timepoints (using the weights in $\phi_{0,1,\dots,n}$ to average the Λ matrices) to estimate how informative the set of
516 neural features containing up to n^{th} order correlations were.

517 We used a permutation-based procedure to form stable estimates of decoding accuracy for each set of
518 neural features. In particular, we computed the decoding accuracy for each of 10 random group assignments
519 of $\mathcal{G}_{\text{train}}$ and $\mathcal{G}_{\text{test}}$. We report the mean accuracy (along with 95% confidence intervals) for each set of neural

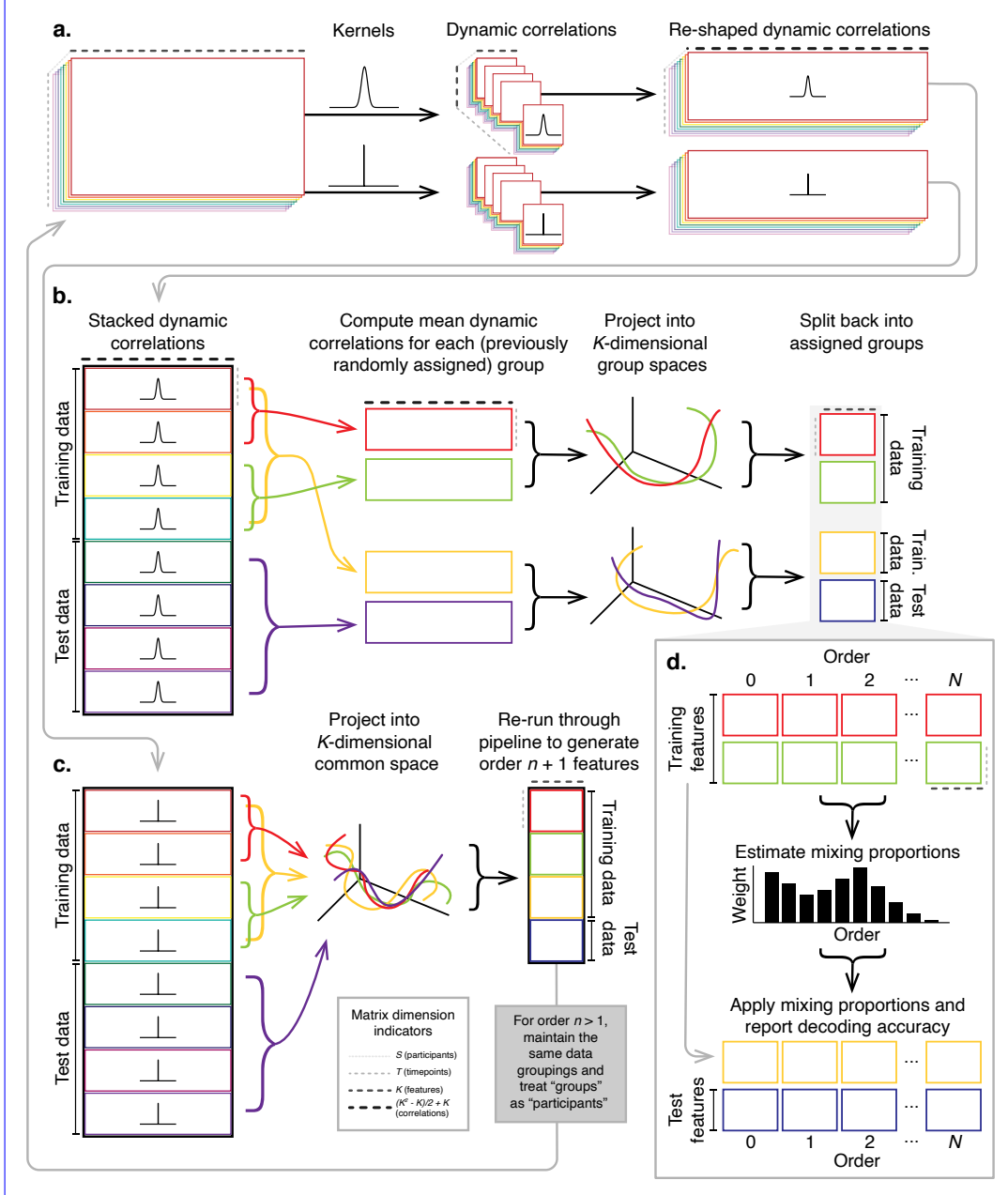


Figure 10: **Decoding analysis pipeline.** **a. Computing dynamic correlations from timeseries data.** Given a timeseries of observations as a $T \times K$ matrix (or a set of S such matrices), we use Equation 4 to compute each participant’s DISFC (relative to other participants in the training or test sub-group, as appropriate). We repeat this process twice—once using the analysis kernel (shown here as a Gaussian in the upper row of the panel), and once using a δ function kernel (lower row of the panel). **b. Projecting dynamic correlations into a lower-dimensional space.** We project the training and test data into K -dimensional spaces to create compact representations of dynamic correlations at the given order (estimated using the analysis kernel). **c. Kernel trick.** We project the dynamic correlations computed using a δ function kernel into a common K -dimensional space. These low-dimensional embeddings are fed back through the analysis pipeline in order to compute features at the next-highest order. **d. Decoding analysis.** We split the training data into two equal groups, and optimize the feature weights (i.e., dynamic correlations at each order) to maximize decoding accuracy. We then apply the trained classifier to the (held-out) test data.

520 features.

521 **Identifying robust decoding results**

522 The temporal decoding procedure we use to estimate which neural features support ongoing cognitive
523 processing is governed by several parameters. In particular, Equation 4 requires defining a kernel function,
524 which can take on different shapes and widths. For a fixed set of neural features, each of these parameters
525 can yield different decoding accuracies. Further, the best decoding accuracy for a given timepoint may be
526 reliably achieved by one set of parameters, whereas the best decoding accuracy for another timepoint might
527 be reliably achieved by a different set of parameters, and the best decoding accuracy across *all* timepoints
528 might be reliably achieved by still another different set of parameters. Rather than attempting to maximize
529 decoding accuracy, we sought to discover the trends in the data that were robust to classifier parameters
530 choices. Specifically, we sought to characterize how decoding accuracy varied (under different experimental
531 conditions) as a function of which neural features were considered.

532 To identify decoding results that were robust to specific classifier parameter choices, we repeated our
533 decoding analyses after substituting into Equation 4 each of a variety of kernel shapes and widths. We
534 examined Gaussian (Fig. 9c), Laplace (Fig. 9d), and Mexican Hat (Fig. 9e) kernels, each with widths of 5, 10,
535 20, and 50 samples. We then report the average decoding accuracies across all of these parameter choices.
536 This enabled us to (partially) factor out performance characteristics that were parameter-dependent, within
537 the set of parameters we examined.

538 **Reverse inference**

539 The dynamic patterns we examined comprise high-dimensional correlation patterns at each timepoint. To
540 help interpret the resulting patterns in the context of other studies, we created summary maps by computing
541 the across-timepoint average pairwise correlations at each order of analysis (first order, second order, etc.).
542 We selected the 10 strongest (absolute value) correlations at each order. Each correlation is between the
543 dynamic activity patterns (or patterns of dynamic high-order correlations) measured at two RBF nodes
544 (see *Hierarchical Topographic Factor Analysis*). Therefore, the 10 strongest correlations involved up to 20 RBF
545 nodes. Each RBF defines a spatial function whose activations range from 0 to 1. We constructed a map
546 of RBF components that denoted the endpoints of the 10 strongest correlations (we set each RBF to have a
547 maximum value of 1). We then carried out a meta analysis using Neurosynth (Rubin et al., 2017) to identify
548 the 10 terms most commonly associated with the given map. This resulted in a set of 10 terms associated
549 with the average dynamic correlation patterns at each order.

550 **Results**

551 We sought to understand whether high-level cognition is supported by dynamic patterns of high-order
552 correlations. To that end, we developed a computational framework for estimating the dynamics of
553 stimulus-driven high-order correlations in multivariate timeseries data (see *Dynamic inter-subject functional*
554 *connectivity (DISFC)* and *Dynamic higher-order correlations*). We evaluated the efficacy of this framework at
555 recovering known patterns in several synthetic datasets (see *Synthetic data*). We then applied the framework
556 to a public fMRI dataset collected as participants listened to an auditorily presented story, listened to a
557 temporally scrambled version of the story, or underwent a resting state scan (see *Functional neuroimaging data*
558 *collected during story listening*). We used the relative decoding accuracies of classifiers trained on different
559 sets of neural features to estimate which types of features reflected ongoing cognitive processing.

560 **Recovering known dynamic correlations from synthetic data**

561 We generated synthetic datasets that differed in how the underlying correlations changed over time. For
562 each dataset, we applied Equation 4 with a variety of kernel shapes and widths. We assessed how well
563 the true underlying correlations at each timepoint matched the recovered correlations (Fig. 2). For every
564 kernel and dataset we tested, our approach recovered the correlation dynamics we embedded into the data.
565 However, the quality of these recoveries varied across different synthetic datasets in a kernel-dependent
566 way.

567 **Recovering known dynamic correlations from synthetic data.** Each panel displays the average
568 correlations between the vectorized upper triangles of the recovered correlation matrix at each timepoint
569 and either the true underlying correlation at each timepoint or a reference correlation matrix. (The averages
570 are taken across 10 different randomly generated synthetic datasets of the given category.) Error ribbons
571 denote 95% confidence intervals (taken across datasets). Different colors denote different kernel shapes,
572 and the shading within each color family denotes the kernel width parameter. For a complete description
573 of each synthetic dataset, see *Synthetic data*. **a. Constant correlations.** These datasets have a stable
574 (unchanging) underlying correlation matrix. **b. Random correlations.** These datasets are generated using
575 a new independently drawn correlation matrix at each new timepoint. **c. Ramping correlations.** These
576 datasets are generated by smoothly varying the underlying correlations between the randomly drawn
577 correlation matrices at the first and last timepoints. The left panel displays the correlations between the
578 recovered dynamic correlations and the underlying ground truth correlations. The middle panel compares
579 the recovered correlations with the *first* timepoint's correlation matrix. The right panel compares the
580 recovered correlations with the *last* timepoint's correlation matrix. **d. Event-based correlations.** These

581 datasets are each generated using five randomly drawn correlation matrices that each remain stable for a fifth
582 of the total timecourse. The left panel displays the correlations between the recovered dynamic correlations
583 and the underlying ground truth correlations. The right panels compare the recovered correlations with the
584 correlation matrices unique to each event.

585 In general, wide monotonic kernel shapes (Laplace, Gaussian), and wider kernels (within a shape),
586 performed best when the correlations varied gradually from moment-to-moment (Figs. 2a, c, and d). In the
587 extreme, as the rate of change in correlations approaches 0 (Fig. 2a), an infinitely wide kernel would exactly
588 recover the Pearson's correlation (e.g., compare Eqns. 1 and 4).

589 When the correlation dynamics were unstructured in time (Fig. 2b), a Dirac δ kernel (infinitely narrow)
590 performed best. This is because, when every timepoint's correlations are independent of the correlations at
591 every other timepoint, averaging data over time dilutes the available signal. Following a similar pattern,
592 holding kernel shape fixed, narrower kernel parameters better recovered randomly varying correlations.

593 Cognitively relevant dynamic high-order correlations in fMRI data

594 We used across-participant temporal decoders to identify cognitively relevant neural patterns in fMRI
595 data (see *Forward inference and decoding accuracy*). The dataset we examined comprised four experimental
596 conditions that exposed participants to stimuli that varied systematically in how cognitively engaging they
597 were. The *intact* experimental condition had participants listen to an audio recording of a 10-minute story.
598 The *paragraph*-scrambled experimental condition had participants listen to a temporally scrambled version
599 of the story, where the paragraphs occurred out of order (but where the same total set of paragraphs were
600 presented over the full listening interval). All participants in this condition experienced the scrambled
601 paragraphs in the same order. The *word*-scrambled experimental condition had participants listen to a
602 temporally scrambled version of the story where the words in the story occurred in a random order.
603 All participants in the word condition experienced the scrambled words in the same order. Finally, in a
604 *rest* experimental condition, participants lay in the scanner with no overt stimulus, with their eyes open
605 (blinking as needed). This dataset provided a convenient means of testing our hypothesis that different
606 levels of cognitive processing and engagement are supported by different orders of brain activity dynamics.

607

608 **Across-participant decoding accuracy varies with correlation order and cognitive engagement. a. Decoding**
609 **accuracy as a function of order: PCA.** Order (x-axis) refers to the maximum order of dynamic correlations
610 that were available to the classifiers (see *Feature weighting and testing*). The reported across-participant
611 decoding accuracies are averaged over all kernel shapes and widths (see *Identifying robust decoding results*).

612 The y -values are displayed relative to chance accuracy (intact: $\frac{1}{300}$; paragraph: $\frac{1}{272}$; word: $\frac{1}{300}$; rest: $\frac{1}{400}$). The
613 error ribbons denote 95% confidence intervals across cross-validation folds (i.e., random assignments of
614 participants to the training and test sets). The colors denote the experimental condition. Arrows denote sets
615 of features that yielded reliably higher (upwards facing) or lower (downward facing) decoding accuracy
616 than the mean of all other features (via a two-tailed test, thresholded at $p < 0.05$). Figure 5 displays additional
617 comparisons between the decoding accuracies achieved using different sets of neural features. The circled
618 values represent the maximum decoding accuracy within each experimental condition. **b. Normalized**
619 **decoding accuracy as a function of order: PCA.** This panel displays the same results as Panel a, but here
620 each curve has been normalized to have a maximum value of 1 and a minimum value of 0 (including the
621 upper and lower bounds of the respective 95% confidence intervals). Panels a and b used PCA to project
622 each high-dimensional pattern of dynamic correlations onto a lower-dimensional space. **c. Decoding**
623 **accuracy as a function of order: eigenvector centrality.** This panel is in the same format as Panel a, but
624 here eigenvector centrality has been used to project the high-dimensional patterns of dynamic correlations
625 onto a lower-dimensional space. **d. Normalized decoding accuracy as a function of order: eigenvector**
626 **centrality.** This panel is in the same format as Panel b, but here eigenvector centrality has been used to
627 project the high-dimensional patterns of dynamic correlations onto a lower-dimensional space.

628 In brief, we computed timeseries of dynamic high-order correlations that were similar across participants
629 in each of two randomly assigned groups: a training group and a test group. We then trained classifiers
630 on the training group's data to match each sample from the test group with a stimulus timepoint. Each
631 classifier comprised a weighted blend of neural patterns that reflected up to n^{th} -order dynamic correlations
632 (see *Feature weighting and testing*). We repeated this process for $n \in \{0, 1, 2, \dots, 10\}$. Our examinations of
633 synthetic data suggested that none of the kernels we examined were "universal" in the sense of optimally
634 recovering underlying correlations regardless of the temporal structure of those correlations. We found a
635 similar pattern in the (real) fMRI data, whereby different kernels yielded different decoding accuracies, but
636 no single kernel emerged as the clear "best." In our analyses of neural data, we therefore averaged our
637 decoding results over a variety of kernel shapes and widths in order to identify results that were robust to
638 specific kernel parameters (see *Identifying robust decoding results*).

639 Our approach to estimating dynamic high-order correlations entails mapping the high-dimensional
640 feature space of correlations (a T by $O(K^2)$ matrix) onto a lower-dimensional T by K matrix. We carried out
641 two sets of analyses that differed in how this mapping was computed. The first set of analyses used PCA
642 to find a low-dimensional embedding of the original dynamic correlation matrices (Fig. 4a,b). The second
643 set of analyses characterized correlations in dynamics of each feature's eigenvector centrality, but did not
644 preserve the underlying activity dynamics (Fig. 4c,d).

645 **Statistical summary of decoding accuracies for different neural features.** Each column displays
646 decoding results for one experimental condition (intact, paragraph, word, and rest). We considered dynamic
647 activity patterns (order 0) and dynamic correlations at different orders (order > 0). We used two-tailed *t*-tests
648 to compare the distributions of decoding accuracies obtained using each pair of features. The distributions
649 for each feature reflect the set of average decoding accuracies (across all kernel parameters), obtained for
650 each random assignment of training and test groups. In the upper triangles of each map, warmer colors
651 (positive *t*-values) indicate that the neural feature indicated in the given row yielded higher accuracy than
652 the feature indicated in the given column. Cooler colors (negative *t*-values) indicate that the feature in
653 the given row yielded lower decoding accuracy than the feature in the given column. The lower triangles
654 of each map denote the corresponding *p*-values for the *t*-tests. The diagonal entries display the relative
655 average optimized weight given to each type of feature, in a decoder that included all feature types (see
656 *Feature weighting and testing*).

657 Both sets of temporal decoding analyses yielded qualitatively similar results for the auditory (non-rest)
658 conditions of the experiment (Fig. 4: pink, green, and teal lines; Fig. 5: three leftmost columns). The highest
659 decoding accuracy for participants who listened to the intact (unscrambled) story was achieved using
660 high-order dynamic correlations (PCA: second-order; eigenvector centrality: fourth-order). Scrambled
661 versions of the story were best decoded by lower-order correlations (PCA/paragraph: first-order; PCA/word:
662 order zero; eigenvector centrality/paragraph: order zero; eigenvector centrality/word: order zero). The
663 two sets of analyses yielded different decoding results on resting state data (Fig. 4: purple lines; Fig. 5:
664 rightmost column). We note that while the resting state times could be decoded reliably, the accuracies
665 were only very slightly above chance. We speculate that the decoders might have picked up on attentional
666 drift, boredom, or tiredness; we hypothesize that these all increased throughout the resting state scan.
667 The decoders might be picking up on aspects of these loosely defined cognitive states that are common
668 across individuals. The PCA-based approach achieved the highest resting state decoding accuracy using
669 order zero features (non-correlational, activation-based), whereas the eigenvector centrality-based approach
670 achieved the highest resting state decoding accuracy using second-order correlations. Taken together, these
671 analyses indicate that high-level cognitive processing (while listening to the intact story) is reflected in
672 the dynamics of high-order correlations in brain activity, whereas lower-level cognitive processing (while
673 listening to scrambled versions of the story that lack rich meaning) is reflected in the dynamics of lower-order
674 correlations and non-correlational activity dynamics. Further, these patterns are associated both with the
675 underlying activity patterns (characterized using PCA) and also with the changing relative positions that
676 different brain areas occupy in their associated networks (characterized using eigenvector centrality).

677 **Top terms associated with the endpoints of the strongest correlations:** Each color corresponds to one
678 order of inter-subject functional correlations. The inflated brain plots display the locations of the endpoints
679 of the 10 strongest (absolute value) correlations at each order, thresholded at 0.999, and projected onto the
680 cortical surface. The lists of terms on the right display the top five Neurosynth terms decoded from the
681 corresponding brain maps for each order. Each row displays data from a different experimental condition.
682 Additional maps and their corresponding Neurosynth terms may be found in the *Supplementary materials*
683 (intact: Fig. S1; paragraph: Fig. S2; word: Fig. S3; rest: Fig. S4).

684 Having established that patterns of high-order correlations are informative to decoders, we next wondered
685 which specific networks of brain regions contributed most to these patterns. As a representative example,
686 we selected the kernel parameters that yielded decoding accuracies that best matched the average accuracies
687 across all of the kernel parameters we examined. Using Figure 4c as a template, the best-matching kernel
688 was a Laplace kernel with a width of 50 (Fig. 9d). We used this kernel to compute a single K by $K^{n^{\text{th}}}$ -order
689 DISFC matrix for each experimental condition. We then used Neurosynth to compute the terms most highly
690 associated with the most strongly correlated pairs of regions in each of these matrices (Fig. 6; see *Reverse*
691 *inference*).

692 For all of the story listening conditions (intact, paragraph, and word), we found that first- and second-order
693 correlations were most strongly associated with auditory and speech processing areas. During intact story
694 listening, third-order correlations reflected integration with visual areas, and fourth-order correlations
695 reflected integration with areas associated with high-level cognition and cognitive control, such as the
696 ventrolateral prefrontal cortex. However, during listening to temporally scrambled stories, these higher-order
697 correlations instead involved interactions with additional regions associated with speech and semantic
698 processing. By contrast, we found a much different set of patterns in the resting-state data. First-order
699 resting-state correlations were most strongly associated with regions involved in counting and numerical
700 understanding. Second-order resting-state correlations were strongest in visual areas; third-order correlations
701 were strongest in task-positive areas; and fourth-order correlations were strongest in regions associated with
702 autobiographical and episodic memory. We carried out analogous analyses to create maps (and decode the
703 top-associated Neurosynth terms) for up to fifteenth-order correlations (Figs. S1, S2, S3, and S4). Of note,
704 examining fifteenth-order correlations between 700 nodes using conventional methods would have required
705 storing roughly $\frac{700^{2 \times 15}}{2} \approx 1.13 \times 10^{85}$ floating point numbers—assuming single precision (32 bits each), this
706 would require roughly 32 times as many bits as there are molecules in the known universe! Although these
707 fifteenth-order correlations do appear (visually) to have some well-formed structure, we provide this latter
708 example primarily as a demonstration of the efficiency and scalability of our approach.

709 **Discussion**

710 We tested the hypothesis that high-level cognition is supported by high-order brain network dynamics.
711 We examined high-order network dynamics in functional neuroimaging data collected during a story
712 listening experiment. When participants listened to an auditory recording of the story, participants exhibited
713 similar high-order brain network dynamics. By contrast, when participants instead listened to temporally
714 scrambled recordings of the story, only lower-order brain network dynamics were similar across participants.
715 Our results indicate that higher orders of network interactions support higher-level aspects of cognitive
716 processing (Fig. 7).

717 **Proposed high-order network dynamics underlying high-level cognition during story listening.**
718 Higher orders of network interactions support higher-level aspects of cognitive processing. When tasks
719 evoke richer, deeper, and/or higher-level processing, this is reflected in higher-order network interactions.

720 The notion that cognition is reflected in (and possibly mediated by) patterns of first-order network
721 dynamics has been suggested by or proposed in myriad empirical studies and reviews. Our study
722 extends this line of work by finding cognitively relevant *higher-order* network dynamics that reflect ongoing
723 cognition. Our findings complement other work that uses graph theory and topology to characterize how
724 brain networks reconfigure during cognition.

725 An open question not addressed by our study pertains to how different structures integrate incoming
726 information with different time constants. For example, one line of work suggests that the cortical surface
727 comprises a structured map such that nearby brain structures process incoming information at similar
728 timescales. Low-level sensory areas integrate information relatively quickly, whereas higher-level regions
729 integrate information relatively slowly. Other related work in human and mouse brains indicates that the
730 temporal response profile of a given brain structure may relate to how strongly connected that structure is
731 with other brain areas. Further study is needed to understand the role of temporal integration at different
732 scales of network interaction, and across different anatomical structures.

733 Another potential limitation of our approach relates to recent work suggesting that the brain undergoes
734 rapid state changes, for example across event boundaries. Shappell et al. (2019) used hidden semi-Markov
735 models to estimate state-specific network dynamics. Our general approach might be extended by considering
736 putative state transitions. For example, rather than weighting all timepoints using a similar kernel (Eqn. 4),
737 the kernel function could adapt on a timepoint-by-timepoint basis such that only timepoints determined to
738 be in the same “state” were given non-zero weight.

739 Identifying high-order network dynamics associated with high-level cognition required several important
740 methods advances. First, we used kernel-based dynamic correlations to extend the notion of (static)

741 inter-subject functional connectivity to a dynamic measure of inter-subject functional connectivity (DISFC)
742 that does not rely on sliding windows, and that may be computed at individual timepoints. This allowed us
743 to precisely characterize stimulus-evoked network dynamics that were similar across individuals. Second,
744 we developed a computational framework for efficiently and scalably estimating high-order dynamic
745 correlations. Our approach uses dimensionality reduction algorithms and graph measures to obtain
746 low-dimensional embeddings of patterns of network dynamics. Third, we developed an analysis framework
747 for identifying robust decoding results by carrying out our analyses using a range of parameter values and
748 then identifying which results were robust to specific parameter choices.

749 **Concluding remarks**

750 The complex hierarchy of dynamic interactions that underlie our thoughts is perhaps the greatest mystery in
751 modern science. Methods for characterizing the dynamics of high-order correlations in neural data provide
752 a window into the neural basis of cognition. By showing that high-level cognition is reflected in high-order
753 network dynamics, we have elucidated the next step on the path towards understanding the neural basis
754 of cognition.

755 **Acknowledgements**

756 We acknowledge discussions with Luke Chang, Vassiki Chauhan, Hany Farid, Paxton Fitzpatrick, Andrew
757 Heusser, Eshin Jolly, Aaron Lee, Qiang Liu, Matthijs van der Meer, Judith Mildner, Gina Notaro, Stephen
758 Satterthwaite, Emily Whitaker, Weizhen Xie, and Kirsten Ziman. Our work was supported in part by NSF
759 EPSCoR Award Number 1632738 to J.R.M. and by a sub-award of DARPA RAM Cooperative Agreement
760 N66001-14-2-4-032 to J.R.M. The content is solely the responsibility of the authors and does not necessarily
761 represent the official views of our supporting organizations.

762 **Author contributions**

763 Concept: J.R.M. Implementation: T.H.C., L.L.W.O., and J.R.M. Analyses: L.L.W.O. and J.R.M. Writing:
764 L.L.W.O. and J.R.M.

765 **References**

- 766 Allen, E. A., Damaraju, E., Plis, S. M., Erhardt, E. B., Eichele, T., & Calhoun, V. D. (2012). Tracking
767 whole-brain connectivity dynamics in the resting state. *Cerebral Cortex*, 24(3), 663–676.
- 768 Alvarez-Hamelin, I., Dall'Asta, L., Barrat, A., & Vespignani, A. (2005). *k*-corr decomposition: a tool for the
769 visualiztion of large scale networks. *arXiv*, cs/0504107v2.
- 770 Baldassano, C., Chen, J., Zadbood, A., Pillow, J. W., Hasson, U., & Norman, K. A. (2017). Discovering event
771 structure in continuous narrative perception and memory. *Neuron*, 95(3), 709–721.
- 772 Barthélémy, M. (2004). Betweenness centrality in large complex networks. *European Physical Journal B*, 38,
773 163–168.
- 774 Bassett, D., Meyer-Lindenberg, A., Achard, S., Duke, T., & Bullmore, E. (2006, December). Adaptive
775 reconfiguration of fractal small-world human brain functional networks. *Proceedings of the National
776 Academy of Sciences, USA*, 103(51), 19518–23.
- 777 Beaty, R. E., Benedek, M., Silvia, P. J., & Schacter, D. L. (2016). Creative cognition and brain network
778 dynamics. *Trends in Cognitive Sciences*, 20(2), 87–95.
- 779 Betzel, R. F., Byrge, L., Esfahlani, F. Z., & Kennedy, D. P. (2019). Temporal fluctuations in the brain's modular
780 architecture during movie-watching. *bioRxiv*, doi.org/10.1101/750919.
- 781 Bonacich, P. (2007). Some unique properties of eigenvector centrality. *Social Networks*, 29(4), 555–564.
- 782 Bullmore, E., & Sporns, O. (2009). Complex brain networks: graph theoretical analysis of structural and
783 functional systems. *Nature Reviews Neuroscience*, 10(3), 186–198.
- 784 Capota, M., Turek, J., Chen, P.-H., Zhu, X., Manning, J. R., Sundaram, N., . . . Shin, Y. S. (2017). *Brain imaging
785 analysis kit*. Retrieved from <https://doi.org/10.5281/zenodo.59780>
- 786 Chang, C., & Glover, G. H. (2010). Time-frequency dynamics of resting-state brain connectivity measured
787 with fMRI. *NeuroImage*, 50, 81–98.
- 788 Chien, H.-Y. S., & Honey, C. J. (2019). Constructing and forgetting temporal context in the human cerebral
789 cortex. *bioRxiv*, doi.org/10.1101/761593.
- 790 Christakis, N. A., & Fowler, J. H. (2010). Social network sensors for early detection of contagious outbreaks.
791 *PLoS One*, 5(9), e12948.

- 792 Combrisson, E., Vallat, R., O'Reilly, C., Jas, M., Pascarella, A., l Saive, A., ... Jerbi, K. (2019). Visbrain: a
793 multi-purpose GPU-accelerated open-source suite for multimodal brain data visualization. *Frontiers in*
794 *Neuroinformatics*, 13(14), 1–14.
- 795 Comon, P., Jutten, C., & Herault, J. (1991). Blind separation of sources, part II: Problems statement. *Signal*
796 *Processing*, 24(1), 11 - 20.
- 797 Demertzi, A., Tagliazucchi, E., Dehaene, S., Deco, G., Barttfeld, P., Raimondo, F., ... Sitt, J. D. (2019). Human
798 consciousness is supported by dynamic complex patterns of brain signal coordination. *Science Advances*,
799 5(2), eaat7603.
- 800 Estrada, E., & Rodríguez-Velázquez, J. A. (2005). Subgraph centrality in complex networks. *Physical Review*
801 *E*, 71(5), 056103.
- 802 Etzel, J. A., Gazzola, V., & Keysers, C. (2009). An introduction to anatomical ROI-based fMRI classification.
803 *Brain Research*, 1281, 114–125.
- 804 Fallon, J., Ward, P., Parkes, L., Oldham, S., Arnatkevičiūtė, A., Fornito, A., & Fulcher, B. D. (2019).
805 Timescales of spontaneous activity fluctuations relate to structural connectivity in the brain. *bioRxiv*,
806 doi.org/10.1101/655050.
- 807 Fong, A. H. C., Yoo, K., Rosenberg, M. D., Zhang, S., Li, C.-S. R., Scheinost, D., ... Chun, M. M. (2019).
808 Dynamic functional connectivity during task performance and rest predicts individual differences in
809 attention across studies. *NeuroImage*, 188, 14–25.
- 810 Freeman, L. C. (1977). A set of measures of centrality based on betweenness. *Sociometry*, 40(1), 35–41.
- 811 Friston, K. (2000). The labile brain. i. neuronal transients and nonlinear coupling. *Phil. Trans. Roy. Soc. Lon.*,
812 355B, 215–236.
- 813 Geisberger, R., Sanders, P., & Schultes, D. (2008). Better approximation of betweenness centrality. *Proceedings*
814 *of the meeting on Algorithm Engineering and Experiments*, 90–100.
- 815 Gershman, S., Blei, D., Pereira, F., & Norman, K. (2011). A topographic latent source model for fMRI data.
816 *NeuroImage*, 57, 89–100.
- 817 Gonzalez-Castillo, J., Caballero-Gaudes, C., Topolski, N., Handwerker, D. A., Pereira, F., & Bandettini, P. A.
818 (2019). Imaging the spontaneous flow of thought: distinct periods of cognition contribute to dynamic
819 functional connectivity during rest. *NeuroImage*, 202(116129).

- 820 Grossberg, S. (1988). Nonlinear neural networks: Principles, mechanisms, and architectures. *Neural
821 networks*, 1(1), 17–61.
- 822 Halu, A., Mondragón, R. J., Panzarasa, P., & Bianconi, G. (2013). Multiplex PageRank. *PLoS One*, 8(10),
823 e78293.
- 824 Hasson, U., Chen, J., & Honey, C. J. (2015). Hierarchical process memory: memory as an integral component
825 of information processing. *Trends in Cognitive Science*, 19(6), 304-315.
- 826 Hasson, U., Yang, E., Vallines, I., Heeger, D. J., & Rubin, N. (2008). A hierarchy of temporal receptive windows
827 in human cortex. *Journal of Neuroscience*, 28(10), 2539-2550. doi: 10.1523/JNEUROSCI.5487-07.2008
- 828 Haxby, J. V., Gobbini, M. I., Furey, M. L., Ishai, A., Schouten, J. L., & Pietrini, P. (2001). Distributed and
829 overlapping representations of faces and objects in ventral temporal cortex. *Science*, 293, 2425–2430.
- 830 Hinton, G. E., & Salakhutdinov, R. R. (2006). Reducing the dimensionality of data with neural networks.
831 *Science*, 313(5786), 504–507.
- 832 Honey, C. J., Kötter, R., Breakspear, M., & Sporns, O. (2007). Network structure of cerebral cortex shapes
833 functional connectivity on multiple time scales. *Proceedings of the National Academy of Science USA*, 104(24),
834 10240–10245.
- 835 Honey, C. J., Thesen, T., Donner, T. H., Silbert, L. J., Carlson, C. E., Devinsky, O., . . . Hasson, U. (2012). Slow
836 cortical dynamics and the accumulation of information over long timescales. *Neuron*, 76, 423-434. doi:
837 10.1016/j.neuron.2012.08.011
- 838 Huth, A. G., de Heer, W. A., Griffiths, T. L., Theunissen, F. E., & Gallant, J. L. (2016). Natural speech reveals
839 the semantic maps that tile human cerebral cortex. *Nature*, 532, 453–458.
- 840 Huth, A. G., Nisimoto, S., Vu, A. T., & Gallant, J. L. (2012). A continuous semantic space describes
841 the representation of thousands of object and action categories across the human brain. *Neuron*, 76(6),
842 1210-1224.
- 843 Jutten, C., & Herault, J. (1991). Blind separation of sources, part I: An adaptive algorithm based on
844 neuromimetic architecture. *Signal Processing*, 24(1), 1–10.
- 845 Kamitani, Y., & Tong, F. (2005). Decoding the visual and subjective contents of the human brain. *Nature
846 Neuroscience*, 8, 679–685.
- 847 Landau, E. (1895). Zur relativen Wertbemessung der Turnierresultate. *Deutsches Wochenschach*, 11, 366–369.

- 848 Lee, C. S., Aly, M., & Baldassano, C. (2020). Anticipation of temporally structured events in the brain.
849 *bioRxiv*, 10.1101/2020.10.14.338145.
- 850 Lee, D. D., & Seung, H. S. (1999). Learning the parts of objects by non-negative matrix factorization. *Nature*,
851 401, 788–791.
- 852 Lerner, Y., Honey, C. J., Katkov, M., & Hasson, U. (2014). Temporal scaling of neural responses to compressed
853 and dilated natural speech. *Journal of Neurophysiology*, 111, 2433–2444.
- 854 Lerner, Y., Honey, C. J., Silbert, L. J., & Hasson, U. (2011). Topographic mapping of a hierarchy of
855 temporal receptive windows using a narrated story. *Journal of Neuroscience*, 31(8), 2906-2915. doi: 10.1523/
856 JNEUROSCI.3684-10.2011
- 857 Liégeois, R., Li, J., Kong, R., Orban, C., De Ville, D. V., Ge, T., ... Yeo, B. T. T. (2019). Resting brain
858 dynamics at different timescales capture distinct aspects of human behavior. *Nature Communications*,
859 10(2317), doi.org/10.1038/s41467-019-10317-7.
- 860 Lin, J. (2009). Divergence measures based on the Shannon entropy. *IEEE Transactions on Information Theory*,
861 37(1), 145–151.
- 862 Lohmann, G., Margulies, D. S., Horstmann, A., Pleger, B., Lepsien, J., Goldhahn, D., ... Turner, R. (2010).
863 Eigenvector centrality mapping for analyzing connectivity patterns in fMRI data of the human brain.
864 *PLoS One*, 5(4), e10232.
- 865 Lurie, D., Kessler, D., Bassett, D., Betzel, R., Breakspear, M., Keilholz, S., ... Calhoun, V. (2018). On the
866 nature of time-varying functional connectivity in resting fMRI. *PsyArXiv*, doi.org/10.31234/osf.io/xtzre.
- 867 Mack, M. L., Preston, A. R., & Love, B. C. (2017). Medial prefrontal cortex compresses concept representations
868 through learning. *bioRxiv*, doi.org/10.1101/178145.
- 869 Mairal, J., Ponce, J., Sapiro, G., Zisserman, A., & Bach, F. R. (2009). Supervised dictionary learning. *Advances
870 in Neural Information Processing Systems*, 1033–1040.
- 871 Mairal, J. B., Bach, F., Ponce, J., & Sapiro, G. (2009). Online dictionary learning for sparse coding. *Proceedings
872 of the 26th annual international conference on machine learning*, 689–696.
- 873 Manning, J. R., Ranganath, R., Norman, K. A., & Blei, D. M. (2014). Topographic factor analysis: a Bayesian
874 model for inferring brain networks from neural data. *PLoS One*, 9(5), e94914.

- 875 Manning, J. R., Zhu, X., Willke, T. L., Ranganath, R., Stachenfeld, K., Hasson, U., ... Norman, K. A. (2018).
876 A probabilistic approach to discovering dynamic full-brain functional connectivity patterns. *NeuroImage*,
877 180, 243–252.
- 878 McInnes, L., Healy, J., & Melville, J. (2018). UMAP: Uniform manifold approximation and projection for
879 dimension reduction. *arXiv*, 1802(03426).
- 880 McIntosh, A. R., & Jirsa, V. K. (2019). The hidden repertoire of brain dynamics and dysfunction. *Network
881 Neuroscience*, doi.org/10.1162/netn_a_00107.
- 882 Mitchell, T., Shinkareva, S., Carlson, A., Chang, K., Malave, V., Mason, R., & Just, M. (2008). Predicting
883 human brain activity associated with the meanings of nouns. *Science*, 320(5880), 1191.
- 884 Newman, M. E. J. (2005). A measure of betweenness centrality based on random walks. *Social Networks*, 27,
885 39–54.
- 886 Newman, M. E. J. (2008). The mathematics of networks. *The New Palgrave Encyclopedia of Economics*, 2, 1–12.
- 887 Nishimoto, S., Vu, A., Naselaris, T., Benjamini, Y., Yu, B., & Gallant, J. (2011). Reconstructing visual
888 experience from brain activity evoked by natural movies. *Current Biology*, 21, 1 - 6.
- 889 Nocedal, J., & Wright, S. J. (2006). *Numerical optimization*. New York: Springer.
- 890 Norman, K. A., Newman, E., Detre, G., & Polyn, S. M. (2006). How inhibitory oscillations can train neural
891 networks and punish competitors. *Neural Computation*, 18, 1577–1610.
- 892 Opsahl, T., Agneessens, F., & Skvoretz, J. (2010). Node centrality in weighted networks: generalizing degree
893 and shortest paths. *Social Networks*, 32, 245–251.
- 894 Park, H.-J., Friston, K. J., Pae, C., Park, B., & Razi, A. (2018). Dynamic effective connectivity in resting state
895 fMRI. *NeuroImage*, 180, 594–608.
- 896 Pearson, K. (1901). On lines and planes of closest fit to systems of points in space. *The London, Edinburgh,
897 and Dublin Philosophical Magazine and Journal of Science*, 2, 559-572.
- 898 Pereira, F., Lou, B., Pritchett, B., Ritter, S., Gershman, S. J., Kanwisher, N., ... Fedorenko, E. (2018). Toward
899 a universal decoder of linguistic meaning from brain activation. *Nature Communications*, 9(963), 1–13.
- 900 Preti, M. G., Bolton, T. A. W., & Van De Ville, D. (2017). The dynamic functional connectome: state-of-the-art
901 and perspectives. *NeuroImage*, 160, 41–54.

- 902 Rao, C. R. (1982). Diversity and dissimilarity coefficients: a unified approach. *Theoretical Population Biology*,
903 21(1), 24–43.
- 904 Reimann, M. W., Nolte, M., Scolamiero, M., Turner, K., Perin, R., Chindemi, G., ... Markram, H. (2017).
905 Cliques of neurons bound into cavities provide a missing link between structure and function. *Frontiers*
906 in *Computational Neuroscience*, 11(48), 1–16.
- 907 Ricotta, C., & Szeidl, L. (2006). Towards a unifying approach to diversity measures: Bridging the gap
908 between the Shannon entropy and Rao's quadratic index. *Theoretical Population Biology*, 70(3), 237–243.
- 909 Roy, D. S., Park, Y.-G., Ogawa, S. K., Cho, J. H., Choi, H., Kamensky, L., ... Tonegawa, S. (2019). Brain-
910 wide mapping of contextual fear memory engram ensembles supports the dispersed engram complex
911 hypothesis. *bioRxiv*, doi.org/10.1101/668483.
- 912 Rubin, T. N., Kyoejo, O., Gorgolewski, K. J., Jones, M. N., Poldrack, R. A., & Yarkoni, T. (2017). Decoding
913 brain activity using a large-scale probabilistic functional-anatomical atlas of human cognition. *PLoS*
914 *Computational Biology*, 13(10), e1005649.
- 915 Rubinov, M., & Sporns, O. (2010). Complex network measures of brain connectivity: uses and interpreta-
916 tions. *NeuroImage*, 52, 1059–1069.
- 917 Schreiber, T. (2000). Measuring information transfer. *Physical Review Letters*, 85(2), 461–464.
- 918 Shappell, H., Caffo, B. S., Pekar, J. J., & Lindquist, M. A. (2019). Improved state change estimation in
919 dynamic functional connectivity using hidden semi-Markov models. *NeuroImage*, 191, 243–257.
- 920 Simony, E., & Chang, C. (2020). Analysis of stimulus-induced brain dynamics during naturalistic paradigms.
921 *NeuroImage*, 216, 116461.
- 922 Simony, E., Honey, C. J., Chen, J., & Hasson, U. (2016). Dynamic reconfiguration of the default mode
923 network during narrative comprehension. *Nature Communications*, 7(12141), 1–13.
- 924 Sizemore, A. E., Giusti, C., Kahn, A., Vettel, J. M., Betzel, R. F., & Bassett, D. S. (2018). Cliques and cavities
925 in the human connectome. *Journal of Computational Neuroscience*, 44(1), 115–145.
- 926 Solomon, S. H., Medaglia, J. D., & Thompson-Schill, S. L. (2019). Implementing a concept network model.
927 *Behavior Research Methods*, 51, 1717–1736.
- 928 Spearman, C. (1904). General intelligence, objectively determined and measured. *American Journal of*
929 *Psychology*, 15, 201–292.

- 930 Sporns, O., & Honey, C. J. (2006). Small worlds inside big brains. *Proceedings of the National Academy of*
931 *Science USA, 103*(51), 19219–19220.
- 932 Thompson, W. H., Richter, C. G., Plavén-Sigray, P., & Fransson, P. (2018). Simulations to benchmark
933 time-varying connectivity methods for fMRI. *PLoS Computational Biology, 14*(5), e1006196.
- 934 Tipping, M. E., & Bishop, C. M. (1999). Probabilistic principal component analysis. *Journal of Royal Statistical*
935 *Society, Series B, 61*(3), 611–622.
- 936 Toker, D., & Sommer, F. T. (2019). Information integration in large brain networks. *PLoS Computational*
937 *Biology, 15*(2), e1006807.
- 938 Tong, F., & Pratte, M. S. (2012). Decoding patterns of human brain activity. *Annual Review of Psychology, 63*,
939 483–509.
- 940 Turk-Browne, N. B. (2013). Functional interactions as big data in the human brain. *Science, 342*, 580–584.
- 941 van der Maaten, L. J. P., & Hinton, G. E. (2008). Visualizing high-dimensional data using t-SNE. *Journal of*
942 *Machine Learning Research, 9*, 2579-2605.
- 943 Vidaurre, D., Abeysuriya, R., Becker, R., Quinn, A. J., Alfaro-Almagro, F., Smith, S. M., & Woolrich, M. W.
944 (2018). Discovering dynamic brain neworks from big data in rest and task. *NeuroImage, 180*, 646–656.
- 945 Zar, J. H. (2010). *Biostatistical analysis*. Prentice-Hall/Pearson.
- 946 Zheng, M., Allard, A., Hagmann, P., & Serrano, M. A. (2019). Geometric renormalization unravels self-
947 similarity of the multiscale human connectome. *arXiv, 1904.11793*.
- 948 Zou, Y., Donner, R. V., Marwan, N., Donges, J. F., & Kurths, J. (2019). Complex network approaches to
949 nonlinear time series analysis. *Physics Reports, 787*, 1–97.